Evidence of an aseismic slip continuously driving the 2017 Valparaiso earthquake sequence

L. Moutote[1], Y. Itoh[2], O. Lengliné[1], Z. Duputel[3], A. Socquet[2]

[1]Institut Terre et Environnement de Strasbourg, UMR7063, Université de Strasbourg/EOST, CNRS, Strasbourg, France.

[2]Université Grenoble Alpes, Université Savoie Mont Blanc, CNRS, IRD, ISTerre, Grenoble, France.

[3]Observatoire Volcanologique du Piton de la Fournaise, Université Paris Cité, Institut de Physique du Globe de Paris, CNRS, F-75005, Paris France.

Key Points:

- We use a high resolution seismic catalog and GPS to investigate seismic and aseismic process before and after the Valparaiso mainshock
- An unusually high seismicity and an aseismic slip is continuously observed from the foreshock sequence up to days after the mainshock
- Rather than a nucleation phase of the mainshock, the slow slip event acts as an aseismic loading of nearby faults during the entire sequence

Corresponding author: Luc Moutote, `lmoutote@unistra.fr`

Abstract

Following laboratory experiments and friction theory, slow slip events and seismicity rate accelerations observed before mainshock are often interpreted as evidence of a nucleation phase. However, such precursory observations still remain scarce and are associated with different time and length scales, raising doubts about their actual preparatory nature. We study the 2017 Valparaiso $M_w = 6.9$ earthquake, which was preceded by aseismic slip accompanied by an intense seismicity both suspected to reflect its nucleation phase. We complement previous observations, which have focused only on precursory activity, with a continuous investigation of seismic and aseismic processes from the foreshock sequence to the post-mainshock phase. By building a high-resolution seismicity catalog and searching for anomalous seismicity rate increases compared to aftershock triggering models, we highlight an over-productive seismicity starting within the foreshock sequence and persisting several days after the mainshock. Using repeating earthquakes and high-rate GPS observations, we highlight a transient aseismic perturbation starting just before the first foreshock and extending continuously after the mainshock. The estimated slip rate is lightly impacted by large magnitude earthquakes and does not accelerate towards the mainshock. Therefore, the unusual seismic and aseismic activity observed during the 2017 Valparaiso sequence might be interpreted as the result of a slow slip event starting before the mainshock and extending beyond it. Rather than pointing to a possible nucleation phase of the 2017 Valparaiso mainshock, the identified slow slip event acts as an aseismic loading of nearby faults, increasing the seismic activity, and thus the likelihood of a large rupture.

Plain Language Summary

Both laboratory experiments and friction theory show that earthquakes do not begin abruptly but are preceded by an accelerating slip associated with a seismicity increase. On the field, however, such precursory observations still remain scarce and are associated with different characteristic time and length scales, raising doubts that they actually reflect the same nucleation phenomena. We study the 2017 Valparaiso $M = 6.9$ earthquake, which was preceded by both a slow slip and an intense seismicity suspected to reflect such nucleation phase. We complement previous studies, that have focused only on precursory activity, with a continuous investigation of seismic and slow slip before and after the mainshock. Using refined earthquake detection tools, we highlight a seismicity excess starting before and persisting several days after the mainshock. Using repeating earthquakes and high-resolution GPS, we show that the slow slip does not accelerate towards the mainshock, but continues after it. Therefore, rather than pointing to a possible accelerating nucleation phase of the Valparaiso mainshock, we suggest that the slow slip drives an enhanced seismic activity that is not mainshock-directed. Within such slow-slip driven seismicity, the probability of triggering a large earthquake (subsequently considered as the mainshock) is increased.

1 Introduction

Both laboratory experiments and friction theory show that earthquake ruptures do not begin abruptly but are preceded by a slow slip phase accelerating over a finite nucleation zone (Das & Scholz, 1981; Dieterich, 1992; Rubin & Ampuero, 2005; Latour et al., 2013; McLaskey, 2019). However, extrapolating the results of these laboratory-derived rate-and-state models to natural faults is not straightforward, as some parameters entering the model definition are not known for large-scale systems (Ampuero & Rubin, 2008; Kaneko & Ampuero, 2011). In particular, the size of the nucleation zone predicted by such models is not well constrained. If the nucleation length is large, the slow, quasi-static, predicted crack-like expansion could be observed on natural faults. On the other hand, an accelerating pulse in a small nucleation zone could be more difficult to detect in practice. The existence and detectability of such nucleation phases before actual earthquakes is thus an important question with direct implications for earthquake prediction and seismic hazard assessment (Brodsky & Lay, 2014).

Recently, with geodetic measurements, several aseismic slip transients have been reported before the occurrence of large earthquakes (Mavrommatis et al., 2014; Ruiz et al., 2014; Radiguet et al., 2016; Socquet et al., 2017; Voss et al., 2018; Marill et al., 2021). In addition to geodetic observations, other observations such as repeating earthquakes are frequently used to support the detection of these aseismic processes (Nadeau & Johnson, 1998; Igarashi et al., 2003; Kato et al., 2012; Mavrommatis et al., 2015; Kato et al., 2016; Uchida, 2019). Because of their timing, preceding large events, these transient aseismic slips are sometimes interpreted as evidence of the mainshock nucleation phase as depicted by theory and laboratory experiments. However, despite the densification of geodetic and seismic networks around active faults, precursory aseismic slip observations still remain scarce. The few examples that have been identified often have large uncertainties in both their location and temporal evolution, making it difficult to infer any acceleration trend as the mainshock approaches. Moreover, there are significant discrepancies in the duration of reported preparatory slip, ranging from a few tens of seconds (Tape et al., 2018) to years before the main rupture (e.g., Mavrommatis et al., 2014; Marill et al., 2021), which raises doubts about whether these observations are actually reflecting the same geophysical process.

On the other hand, many large earthquakes are also preceded by seismicity rate increases, which may be additional evidence of a slow preparatory process before large earthquakes (Dodge et al., 1995, 1996; Bouchon et al., 2011, 2013; Seif et al., 2019). In the framework of a slow nucleation phase, such foreshock activity is interpreted as small locked asperities that break up as the background aseismic slip accelerates (Ohnaka, 1992; Dodge et al., 1996; McLaskey, 2019). However, analyzing solely the seismicity rate to infer preparatory process before large earthquake is a difficult task (Ross et al., 2019; van den Ende & Ampuero, 2020; Moutote et al., 2021). Indeed, earthquakes are strongly time- and space-clustered (Helmstetter & Sornette, 2003; Marsan & Lengline, 2008) mainly because they interact with each other, making their probability of occurrence dependent on the past seismic activity. Therefore, the successive occurrence of earthquakes and their interactions can lead to seismicity rate increases, independently from any external process (Helmstetter & Sornette, 2003; Felzer et al., 2004; Marsan & Enescu, 2012). Therefore, determining if the rise of foreshock earthquake sequence results uniquely from earthquake interactions or could in some occasion represent a true signal associated with a preparatory phase remains actively debated (Llenos et al., 2009; Mignan, 2015; Kato et al., 2016; Tape et al., 2018; Ellsworth & Bulut, 2018; Gomberg, 2018).

It is worth mentioning that detecting both an aseismic slip and an enhanced earthquake activity before a large earthquake may not appear as sufficient evidence of a nucleation phase. There are indeed multiple evidence of earthquake swarms that have been linked to a slow slip transient without culminating into a large rupture (Lohman & McGuire, 2007; Vallée et al., 2013; Nishikawa et al., 2021). An interesting example was reported near the Guerrero gap, Mexico, where at least 4 episodic and co-located aseismic slip events have been successively detected over 10 years without being followed by any significant earthquake. Yet, in 2014, a slow slip event was reported on the same portion of the interface but was this time associated with the $M_w = 7.3$ Papanoa earthquake (Radiguet et al., 2016). Such example shows that detecting both an aseismic slip and an unusually high seismicity before a large earthquake may not necessarily represent a deterministic nucleation process of a mainshock.

In this study, we analyze in detail the seismic and aseismic processes observed before and after the April 2017 Valparaiso $M_w = 6.9$ earthquake (Chile; Figure 1). This mainshock was preceded by an intense 2-day long foreshock sequence with magnitudes up to $M_w = 6$ and followed by an abundant aftershock activity. In addition, an aseismic precursory fault slip has been reported during the foreshock sequence (Ruiz et al., 2017; Caballero et al., 2021). This aseismic pre-slip may have initiated before the first foreshock and is persisting, at least, up to the mainshock (Caballero et al., 2021). However, the aseismic activity was not investigated after the mainshock and its onset and time evolution is still unclear due to the sampling intervals of the GPS data used (6 hours and 1 day, respectively). We, first, build a high-resolution seismic catalog from 2016 to 2021 and then we compare the seismicity in the vicinity of the mainshock with aftershock triggering models to highlight unusual variations in seismicity rates. In a second part, we investigate the aseismic slip transient during the entire earthquake sequence using repeating earthquake and high-rate GPS observation. We finally discuss whether the aseismic slip is part of the nucleation of the mainshock or if it just mediates the whole seismic sequence.

2 ValEqt: A high resolution catalog

In order to produce a detailed analysis of the micro-seismic activity near the mainshock, we build a high resolution catalog using newly developed detection methods. We use 13 broadband stations from the National Seismological Center (CSN) of the University of Chile (Barrientos & National Seismological Center (CSN) Team, 2018) in the vicinity of the mainshock from 1 January 2016 to 1 January 2021 (see Figure 1). Only a few stations were available earlier than 2016, which does not allow us to carry out a reliable seismicity analysis.

2.1 Detection, location and magnitude estimation

We pick P- and S- wave arrivals of earthquakes on daily raw waveforms using EQTransformer, an automatic deep learning phase picker trained on a worldwide earthquake database (Mousavi et al., 2020a). We associate phases picks into events with REAL (Zhang et al., 2019a), performed over a 3° by 3° grid. We only consider events for which both P and S phases are associated on at least 3 stations. We locate events using NonLinLoc (Lomax et al., 2000) in a 3D velocity model of Chile (B. Potin, pers. com.). We discard events with a NonLinLoc RMS residual above 1s to avoid false detections.

We then estimate a local magnitude following the original Richter approach on Wood-Anderson seismometers. For that purpose, we correct the recorded waveforms from their instrument response and convolve them with a Wood-Anderson response. For all stations and horizontal components, we convert the maximum zero to peak S waves amplitude, A_{WA}, into a magnitude, M, using the Richter empirical formula (Richter, 1935, 1958; Shearer, 2019):

$$M = \log_{10}(A_{WA}) - 2.21 + 2.56\log_{10}(\Delta) \tag{1}$$

where A_{WA}, is in mm and Δ is the hypocentral distance in km. The event magnitude is taken as the median of all estimations over stations/components. Given its proximity to the ocean, the Valparaiso region is prone to oceanic microseismic noise that dominates the S wave amplitude of small events. To reduce the noise level, we thus first filter all waveforms between 1 and 20 Hz prior to the magnitude estimation. If an event is estimated with a magnitude $M > 3$, we re-estimate its magnitude accounting for lower frequencies with a 0.05-20 Hz bandpass filtering.

The resultant catalog consists of more than 90 000 events from 2016 to 2021 within a 3 by 3 degree region centered on the Valparaiso mainshock. Over the same region and period, the official Chilean catalog (Centro Seismologico National, CSN) reported only $\sim$7000 events. Figure 1 shows the spatial and temporal distribution of earthquakes according to this catalog.

figures/Main/map.pdf

Figure 1. Time, location and magnitude of earthquakes detected by our Valparaiso high resolution catalog between 2016 and 2021. a) Horizontal location of earthquakes. The red triangles show the location of the 13 broadband stations used to build the catalog. b) Time evolution of the latitude of earthquakes. c) Depth and longitude of earthquakes. The thick red line shows the extent of the ValEqt catalog analyzed in this study. d) Time and magnitude of earthquakes within the ValEqt sub-region. Black dots are our catalog. Blue dots (in the foreground) are the CSN catalog used as reference. e) Gutenberg-Richter magnitude frequency distribution of our ValEqt catalog in black and the CSN catalog in blue. f) Same as d) but zoomed in the vicinity of the mainshock. g) Comparison of magnitude estimations for earthquakes shared by the CSN and the ValEqt catalog. The blue star indicates the $M_w = 6.9$ mainshock.

2.2 Event selection and comparison with the CSN catalog

To study the seismic activity in the vicinity of the mainshock, we extract all the earthquakes within $-33.5° \leq Latitude \leq -32.8°$ and $-72.5° \leq Longitude \leq -71.5°$ with no depth cutoff. Our goal here is to focus on seismicity in the vicinity of the mainshock that is not affected by other nearby large earthquakes. From Figure 1.b we see several temporally clustered seismic activity. The largest cluster is related to the 2017 $M_w = 6.9$ Valparaiso mainshock. We clearly see that none of the secondary clusters affect our sub-catalog. Figure 1.c shows the depth distribution of earthquakes along longitude that clearly highlight the subduction plane. The 2017 activity is located on the shallowest part of the subduction plane with no direct connection with deeper activities. This sub-catalog (hereafter, referred to ValEqt catalog) gathers more than 10000 events. The magnitude evolution as a function of time of ValEqt is presented in black in Figure 1.d and a zoom on the mainshock sequence in Figure 1.f.

We compare our ValEqt catalog with the CSN catalog (blue in Figures 1.d and .f) from the same sub-region. The Gutenberg-Richter distribution in Figure 1.e shows that the ValEqt catalog includes much more small magnitude earthquakes than the CSN catalog, lowering the local magnitude of completeness from $M_c^{CSN} = 3$ to $M_c^{ValEqt} = 2$. We note that almost all CSN earthquakes were re-detected by our detection procedure. We only miss 12 CSN earthquakes all with a magnitude below 3, either because the data of the 13 stations used in our study were unavailable at that time or these earthquakes were interlaced with the waveform of a preceding earthquake making difficult to pick P and S phases even after a careful review. On the other hand, thanks to EQTransformer, we detected many earthquakes with a magnitude above 3 not listed in CSN catalog. These newly identified earthquakes occurred immediately before or after a larger earthquake, making them difficult to detect by standard methods (i.e. STA/LTA or visual inspection) because of the amplitude ratio. Figure 1.g shows the differences in magnitude for earthquakes recorded in both catalogs. Overall, ValEqt magnitudes are consistent with CSN estimations, but with a constant bias of about +0.2 units. This shift could result from a different relation used by CSN to compute earthquakes magnitude compare to Equation 1. Because local magnitude saturates for large magnitude earthquakes, the mainshock magnitude is underestimated at $M = 6.2$. We, therefore, fix manually its value based on its moment magnitude $M_w = 6.9$.

3 Seismicity analysis

The high resolution ValEqt catalog allows us to obtain a refined view of the seismicity rate variations observed in the region before and after the $M_w = 6.9$ Valparaiso mainshock. The two largest foreshocks are recorded with $M = 6.1$ and $M = 5.5$, approximately 2 days and 1 days before the mainshock, respectively. The largest aftershock occurred 4 days after the mainshock with a magnitude $M = 6.1$.

Because of its space and time correlation with the mainshock, a previously reported slow slip event during the foreshock sequence (Ruiz et al., 2017; Caballero et al., 2021) is suspected to reflect the nucleation process of the $M_w = 6.9$ earthquake and to possibly drive the foreshock seismicity. However, sharp increase of the seismicity rate following the two largest foreshocks in Figure 2.a suggests that part of the foreshock activity is not directly linked with the slow slip event and actually corresponds to aftershock triggering. We, therefore, estimate which part of the seismicity before and after the $M_w = 6.9$ mainshock could be explained by aftershock triggering. For that, we use two temporal models of aftershock triggering: the Epidemic Type Aftershock Sequence (ETAS) model (Ogata, 1988; Zhuang et al., 2012) and a Model Independent Stochastic Declustering approach (Marsan & Lengline, 2008). We focus only on the temporal variations of the seismicity because the studied region is sufficiently small, isolated and uniquely clustered compared to the location uncertainties of earthquakes.

figures/Main/ETASI.pdf

Figure 2. (a) Time-evolution of the cumulative number of earthquakes observed in the ValEqt catalog (black) and predicted by the best fitting ETASI model (blue) around the mainshock time. The blue dotted line shows the ETASI 99^{th} percentile confidence interval. The middle subplot is the difference between the blue and black lines. Black dots in the bottom subplot indicate the time-magnitude evolution of the ValEqt catalog. (b) same as (a) but for the full 5-years period and with the transformed-time domain axis (Ogata, 1988). The blue star indicates the mainshock. Note how the transformed time domain allows an efficient analysis of the full 5-years seismicity with respect to the ETASI model.

3.1 ETAS and short-term incompleteness

The ETAS model has been widely used to generate synthetic earthquake catalogs (Zhuang & Touati, 2015). It can serve as a basis for establishing a reference earthquake catalog and testing any deviation from it (Ogata, 1989, 1992; Marsan et al., 2014; Moutote et al., 2021; Seif et al., 2019). It is also used to forecast seismicity (Zhuang, 2012; Taroni et al., 2018). The ETAS model is a superposition of a stationary background seismicity term and aftershock activity scaled in intensity by the magnitude of the triggering event. The conditional intensity $\lambda_0(t)$ (i.e. the expected seismicity rate at t) given by the ETAS model can be written as:

$$\lambda_0(t) = \mu + \sum_{i|t_i<t} A\mathrm{e}^{\alpha(M_i-M_c)}(t-t_i+c)^{-p}, \tag{2}$$

where μ is the stationary background seismicity rate. The sum on the right hand side of this equation describes the expected aftershock seismicity rate at time t, triggered by all the preceding events. The parameters c and p describe the time-decay in the aftershock seismicity rate (Omori, 1895; Utsu et al., 1995). The intensity of the triggering is scaled by A and α, the global aftershock productivity of the region and the magnitude dependence in the number of triggered events, respectively. M_c is the magnitude of completeness. In the ETAS model, magnitudes are independent and distributed according to Gutenberg-Richter's law (G-R). We can write the G-R probability density function as:

$$f_0(M) = \beta\mathrm{e}^{-\beta(M-M_c)} \tag{3}$$

$\beta = b\ln(10)$, with b the b-value of the G-R law. The G-R law and the ETAS model are only defined above the magnitude of completeness M_c that is supposed to be constant over time. However, in actual seismicity catalogs, we frequently observe temporal variations of M_c (Kagan, 2004; de Arcangelis et al., 2018; Hainzl, 2016). Such variations of M_c are usually attributed to the lack of low magnitude earthquakes during network maintenance or during period of high seismic activity. The latter is our main concern for the ValEqt catalog since the data availability is quite constant over the studied time-period. When the seismicity rate is high, records of seismic wave of low magnitude earthquakes are likely to be hidden by larger magnitude events. As shown in Figure 1.e, we estimate an average magnitude of completeness $M_c = 2$ for the ValEqt catalog over 5 years. However, M_c can increase just after large earthquakes because of the numerous aftershocks they trigger. This is illustrated in Figure 3, showing a deficiency in small magnitude earthquakes in the first hour following the $M_w = 6.9$ Valparaiso earthquake, with a magnitude of completeness rising up to $M_c \sim 3.5$ immediately after the mainshock. The observed $M \geq 2$ earthquake rate is, therefore, underestimated just after the mainshock, which may bias the estimation of an ETAS magnitude-dependent triggering process. This figures/Main/incompletness.pdf

Figure 3. Short-term incompleteness after the Valparaiso mainshock. The red horizontal line is the average magnitude of completeness (M_c) estimated from the G-R distribution of the ValEqt catalog. Note the lack of low magnitude earthquakes above M_c during early aftershock times. The blue star indicate the mainshock.

bias is often referred to as Short-Term Incompleteness because it is visible just after large earthquakes (Kagan, 2004; de Arcangelis et al., 2018; Hainzl, 2016). However, it can be generalized to a Rate-dependent incompleteness (Hainzl, 2021) since missing low magnitude events can affect any time-window with a sufficiently high seismicity rate.

To accommodate our seismicity analysis with $M_c = 2$ while taking into account the rate-dependent incompleteness, we use the ETASI model (i.e. ETAS-Incomplete; Hainzl (2016, 2021)) instead of the ETAS model. This new formulation takes into account a rate-dependent incompleteness by adding one parameter T_b, defined as a blind time; for a duration T_b following an earthquake of magnitude M, any event of magnitude less than M cannot be detected. In practice, the ETASI model acts as an apparent rate at every t, considering the likelihood of observing large magnitude events in $[t - T_b, t]$. The ETASI apparent seismicity rate function is (Hainzl, 2021):

$$\lambda(t) \quad \approx \quad \frac{1}{T_b}(1 - \mathrm{e}^{-T_b \lambda_0(t)}). \tag{4}$$

From equation 4, we see that the ETASI rate $\lambda(t)$ is simply the original ETAS rate $\lambda_0(t)$ of (2) modulated by the blind time T_b during high seismicity rate periods. Likewise, the G-R distribution is affected by the rate-dependent incompleteness because some low magnitude earthquakes are undetected. The apparent Gutenberg-Richter distribution at t is (Hainzl, 2021):

$$f(m,t) \quad \approx \quad \beta T_b \lambda_0(t) \frac{\mathrm{e}^{-\beta(M-M_c)} \mathrm{e}^{T_b \lambda_0(t) \mathrm{e}^{-\beta(M-M_c)}}}{1 - \mathrm{e}^{-T_b \lambda_0(t)}} \tag{5}$$

From a given catalog ($t_i \in [T_1, T_2], m_i \geq M_c$), we extract the best fitting ETASI parameters by maximizing the following Log-Likelihood function (Hainzl, 2021):

$$\mathcal{LL} = \sum_{i=1}^{N} \ln[f(m_i, t_i)] + \sum_{i=1}^{N} \ln[\lambda(t_i)] - \int_{T_1}^{T_2} \lambda(t)\,\mathrm{d}t \tag{6}$$

For the ValEqt catalog, we extract the best fitting parameters for magnitudes above the magnitude of completeness $M_c = 2$. Moreover, following Davidsen and Baiesi (2016), we impose self similarity in the aftershock triggering process by fixing $\alpha = \beta$ during the maximization of the likelihood function. With this self similarity constraint, the probability for a $M = 8$ to trigger $M = 6$ earthquakes is assumed same as the probability for a $M = 4$ to trigger $M = 2$ earthquakes. We tested a case without $\alpha = \beta$ at the earlier stage of this study, but the resultant branching rate inverted from the ValEqt catalog was much larger than 1, leading to a non-stationary synthetic ETAS catalog with an infinite number of aftershocks and increasingly large magnitudes. Fixing $\alpha = \beta$ also reduces the parameters space to 6 parameters as for the classic ETAS model. We present on table 1 the best fitting ETASI parameters extracted from the ValEqt catalog.

To test the reliability of the ETASI Log-Likelihood maximization, we invert the ETASI parameters for 100 synthetics ETASI catalogs (Figure S1). We use the ETASI parameters extracted from ValEqt as the true parameters to generate the synthetic catalogs.

Table 1. Best fitting ETASI parameters extracted from the ValEqt catalog

Parameter	A	c (Minutes)	p	$\alpha = \beta$	μ (events/day)	T_b (seconds)
Value	9.9e−3	11.74	1.18	1.71	0.27	116.57

Results indicate that $A, p, \alpha = \beta$, μ and T_b are well constrained by the parameter estimation and c slightly overestimated but with a reasonably close value. This tendency agrees with the conclusions of Hainzl (2021). They have found a similar bias for c and suggested that it may be explained by the lack of earthquakes during rate-dependent incompleteness. Such incomplete data is breaking the triggering links between earthquakes and complicates the estimation of an Omori-Utsu rate decay for individual aftershock sequences. Moreover, after a large magnitude earthquake, the early aftershock rate is mainly controlled by the rate-dependent incompleteness for a period greater than c. It delays the apparent start of the Omori-Utsu rate decay and likely bias the c-value estimation toward higher values. In any case, as suggested by Hainzl (2021), the c-value estimated with the ETASI model is less biased than estimated with the classic ETAS model over incomplete catalogs.

3.2 Testing ValEqt against the ETASI model

With the best-fitting parameters and Equation 4, we compute the seismicity rate expected by ETASI at any time t in the studied time-period. Integrating this expected seismicity rate over time gives an expected number of earthquakes. We define as $\tau(t)$ the cumulative number of earthquakes expected from the best fitting ETASI model as:

$$\tau(t) = \int_{T_1}^{t} \lambda(u)\,\mathrm{d}u \tag{7}$$

Where, λ is the ETASI rate given by Equation 4 and T_1 is the start time of the catalog. We compare $\tau(t)$ with the observed cumulative number of earthquakes at t, $N_{obs}(t)$. If the best fitting ETASI model explains perfectly the observed seismicity, $\tau(t)$ and $N_{obs}(t)$ must be equal over time. Any strong differences between $\tau(t)$ and $N_{obs}(t)$ highlight an anomalous activity in respect to the ETASI model. Representing the predicted seismic activity, $\tau(t)$ as a function of the observed seismic activity, $N_{obs}(t)$ is known as the transformed time analysis introduced by Ogata (1988).

The evolution of $\tau(t)$ and $N_{obs}(t)$ around the mainshock occurrence time is displayed in Figure 2.a. On Figure 2.b, we display the entire period in the transformed time domain. This transformed time representation enables a simplified comparison of the seismicity over the full duration of the catalog, by gathering periods of low and high seismicity in a single figure. In the transformed time domain, if the seismicity is perfectly explained by the best-fitting ETASI process, $\tau(t)$ and $N_{obs}(t)$ should be equal and thus exhibit a straight line with a slope of 1 (i.e. a unit Poisson rate) with a normal standard deviation of $\sigma(t) = \sqrt{\tau(t)(1 - \frac{\tau(t)}{\tau(T_2)})}$ (Ogata, 1992). If the curve significantly diverges from this straight line, we can interpret the local slope as a seismicity deficit (slope $<$ 1) or excess (slope $>$ 1) compared to the ETASI model. They are better illustrated by the difference $N_{obs}(t) - \tau(t)$ (Figure 2), in which the seismicity deficit and excess correspond to negative and positive slopes, respectively. Our results highlight that the seismicity surrounding the Valparaiso mainshock diverges from the ETASI prediction by more than 3σ. We observe three main regimes of seismicity with respect to the best-fitting ETASI model. From the starting time of the catalog and up to the first foreshock, we observe a low negative slope that indicates a small deficit of earthquakes compared to ETASI model. We then observe a significant change toward a positive slope (step $\geq 3\sigma$) highlighting an excess of seismicity, starting within the foreshock sequence and persisting at least 5 days after the mainshock. After that time, the slope slowly returns to its initial low deficit regime. These results indicate that the best fitting ETASI model cannot successfully reproduce the 5-year seismicity variations observed in the area of the 2017 Valparaiso mainshock. Specifically, they suggest that the anomalously high seismic activity observed from -1 day up to +5 days after the mainshock is driven by a specific process that is not captured by our stationary ETAS model. Moreover, the two deficit time periods can also be explained by this enhanced earthquake activity around the mainshock. This transient enhanced seismicity biases the estimation of ETASI parameters towards higher productivity values than required for the time outside the transient, leading to an overestimation of the seismicity rate. This interpretation is supported by synthetic tests which show that similar variations of $N_{obs}(t)$ - $\tau(t)$ are obtained when a finite duration transient seismic activity is added over the stationary background rate of synthetic catalogs (see Text S1 and Figure S2).

3.3 Declustering approach

To confirm whether the anomalously high seismic activity around the mainshock is a real and significant feature, we employ another declustering approach, which is a modified version of the model-independent stochastic declustering (MISD) algorithm of Marsan and Lengline (2008). Our method differs from the original MISD in two aspects: First, as did for the ETAS model, we focus on the temporal variations of the seismicity rate by ignoring the spatial dependence. Second, in addition to the magnitude-dependent aftershock seismicity and the stationary background seismicity, we consider an external forcing process that can trigger an additional seismicity around the mainshock. It models seismicity unrelated to earthquake interaction, such as slow slip driven seismicity. Neglecting any spatial dependence in the original method, the earthquake rate at time t can be expressed as

$$\phi(t) = \phi_0 + \sum_{i,t_i<t} g(m_i, t - t_i) \tag{8}$$

where ϕ_0 is a constant background rate over the whole duration of the catalog T; m_i and t_i are the magnitude and occurrence time of earthquake i, respectively, and g is a triggering kernel. The method assumes no shape for g but simply considers a piecewise constant discretization in time and magnitude of the kernel such that

$$g_{kl} = g\left(M_k < m < M_{k+1}, T_l < t < T_{l+1}\right) \tag{9}$$

where T_l, and M_k are the time and magnitude intervals used for discretization, respectively. Based on equation (8) and an initial guess of g, we can compute the earthquake rate $\phi(t)$ and then the weights ω_{ij} of earthquake i triggering earthquake j and the background weight ω_{0j}. These weights are defined as

$$\omega_{ij} = \frac{g(m_i, t_j - t_i)}{\phi(t_j)}\,;\, \omega_{0j} = \frac{\phi_0}{\phi(t_j)}, \tag{10}$$

$$\sum_{i=1}^{j-1} \omega_{ij} + \omega_{0j} = 1. \tag{11}$$

where the last equation is used for normalization and actually transforms these weights into probabilities. These weights are then used to compute a new estimate of the triggering kernel and the background rate. The process is repeated until reaching the convergence. For a detailed description of the algorithm, the reader is referred to Marsan and Lengliné (2010).

Then, we further modify the original method without spatial dependence explained above to account for a possible additional seismicity driven by an external process. We assume that this external forcing process starts at the time, t_e and lasts for a duration

T_e. We hypothesize that the contribution of this external process can be modeled with a constant earthquake rate, ϕ_e such that the seismicity rate is now described as

$$\phi(t) = \phi_0 + \sum_{i,t_i<t} g(m_i, t - t_i) + \phi_e \left(\mathcal{H}(t - t_e) - \mathcal{H}(t - t_e - T_e)\right) \tag{12}$$

where $\mathcal{H}$ is the Heaviside step function. We do not attempt to model the shape of this external triggering process but rather keep a simplified model with a constant rate. Therefore, we introduce the weights $\omega_{ej} = \phi_e/\phi(t_j)$ if $t_e < t_j < t_e + T_e$ and 0 otherwise. The normalization condition becomes $\sum_{i=1}^{j-1} \omega_{ij} + \omega_{0j} + \omega_{ej} = 1$. This additional triggering modifies the likelihood function associated with the original algorithm such that we have now:

$$L = -\phi_0 T - \phi_e T_e + n_0 \phi_0 + n_e \phi_e - \sum_{ij} n_i g_{ij} \delta t_j + \sum_{ij} n_{ij} \ln\left(g_{ij}\right), \tag{13}$$

with, n_0 the number of background earthquakes, $n_0 = \sum_i \omega_{0i}$ and $n_e = \sum_i \omega_{ei}$ the number of earthquakes triggered by the external forcing process. The number of earthquakes with magnitude in the interval $[m_i, m_i{+}1]$ is noted n_i, while n_{ij} is the number of earthquakes triggered by a magnitude i earthquake in the time interval $[t_j,\, t_{j+1}]$ of duration δ_j. Based on this approach, we compute the background rate ϕ_0, the kernel g and the external forcing rate, ϕ_e. As the duration of this external forcing T_e is unknown, we simply estimate it by grid search ranging from 0.01 day up to 30 days, and, for each run, we store the inverted parameters as well as the likelihood function returned by the algorithm. We select as the best set of parameters the ones that maximize L, thus fixing as well the duration T_e of the transient. In order to test the method, we perform a series of synthetic tests to check the ability of the proposed algorithm to recover a transient episode of seismicity (See Text S2 and Figure S3).

We apply the declustering algorithm described above to the ValEqt catalog with $t_e = 47$ hours before the occurrence of the Valparaiso mainshock (i.e. the origin time of the first foreshock). We also take into account the time-evolution of the magnitude of completeness following large earthquakes using the approach of Peng et al. (2007) in which a transient magnitude of completeness $m_c(t) = \overline{m}(t) - 1/(b \ln(10))$ is computed with $\overline{m}(t)$ an average magnitude computed over the next N_e earthquakes in time. It follows that an earthquake at time t counts as $n(t) = 10^{m_c(t)-m_c}$. Here, we set $b = 0.74$ as inverted from the ETASI procedure, $m_c = 2$ and we choose $N_e = 10$ as in Marsan and Lengliné (2010). The maximum likelihood, L is obtained with a value of $T_e = 10$ days, corresponding to an inverted value of ϕ_e= 41 earthquake per day. Such large values of transient duration and rate indicate that a substantial part of the seismicity is not well explained by magnitude-dependent triggering kernels alone. Figure 4 shows the background events and those triggered by the external process (i.e., events that do not result from earthquake interactions). This shows that an additional triggering, starting before the Valparaiso mainshock and lasting several days after its occurrence is needed in order to correctly represent the seismicity.

4 Repeater activity

A slowly creeping subducting interface loads embedded asperities that will repeatedly fail over time, producing repeating earthquakes (i.e., with similar source location and waveforms; Uchida (2019); Kato et al. (2012, 2016)). Such repeater events can then be used to track the aseismic slip rate surrounding the ruptured asperities.

To search for repeating events in the vicinity of the 2017 Valparaiso earthquake, we evaluate the similarity of waveforms for all earthquake pairs within the ValEqt catalog. We compute an average cross-correlation coefficient (CC) over the 7 stations that are associated with the largest number of P and S picks (i.e., MT01, MT09, MT02, VA03, figures/Main/MISD.pdf

Figure 4. a) (red) Cumulative count of earthquakes predicted by our best fitting modified MISD model. (black) Cumulative number of earthquakes of the ValEqt catalog. (blue) Cumulative count of earthquake declustered by the modified MISD analysis. This include background events and those triggered by the external process ($\sum_i \omega_{0i} \quad + \quad \omega_{ei}$). Bottom subplot (black dot) shows times and magnitudes of the ValEqt catalog. b) Same as a) but zoomed in the Grey area. t_e and T_e are respectively the start time and the duration of the external process of our modified MISD model.

VA06, MT07 and VA05). At every station, the cross-correlation coefficient is defined as the maximum value of the cross-correlation function between the two waveforms of the earthquake pair. This cross-correlation function is computed in a 40-second time window starting 5 seconds before the P arrival and in the 2 to 20 Hz band. This allows us to include both P and S arrivals and to maximize the signal to noise ratio. The final CC value of the earthquake pair is defined as the average of the CC values computed at available stations. Pairs of events that share less than 3 stations are automatically discarded. Then, we gather earthquakes with similar waveforms into families based on a hierarchical clustering algorithm using a complete linkage over the CC value. We retain families of earthquakes with a high waveform similarity (i.e. $CC > 0.80$) as a first sub-set of potential repeating earthquakes. Then, we ensure that events within a family are all co-located on the same asperity using the HypoDD double-difference relocation algorithm (Waldhauser & Ellsworth, 2000). For every pair of event, we use travel time differences between both P and S phases at all stations. The time delay between 2 P phases is estimated with the maximum of the cross correlation function over 5 second windows that start 1.5 second before the pick. For S phases, we use a 10 second window starting 3 second before the pick. Those traces were band-pass filtered with a band width of 2-20 Hz. To evaluate the relocation uncertainties, we relocate events within each family using the SVD solving method of HypoDD. On average, a pair of event is relocated with 13 differential travel-time measurements and all families with unsuccessful HypoDD solution are discarded. After the relocation, we estimate a rupture radius for each event within the remaining families by assuming a circular crack model and a stress drop of 3 MPa (Hanks & Bakun, 2002). With relocated hypocenters and circular rupture radii, we compute the 3D distance between rupture patches for every earthquake pairs. Taking into account hypocenter location uncertainties, we discard all events that have less than 80% of chance to intersect with all the other rupture areas of the family. Finally, we discard events within a family with a magnitude difference $\Delta M \geq 1$. With these criteria, all the events in each repeater family have a high waveform similarity and they are sufficiently collocated considering their rupture size with a similar magnitude.

Following this approach, we detected more than 350 repeater families including at least 2 events (Figures 5 and 6). Across all families, we identified more than 1200 repeating earthquakes. In order to test the robustness of our repeating earthquake analysis, we changed the various thresholds for forming the repeater sequences. It yielded moderate variation of the number of repeaters and number of families but does not alter the conclusions presented below. An intense repeater activity initiated during the 2-days foreshock sequence and it presents the highest observed repeater rate over the whole catalog duration. After the mainshock occurrence time, the repeater rate decays continuously over the whole analyzed period, but never returns to its initial rate. Unlike the seismicity of the ValEqt catalog, the repeaters rate is not strongly impacted by the occurrences of large magnitude earthquakes.

figures/Main/repeaters.pdf

Figure 5. (a) Families of repeating earthquake detected in the ValEqt catalog. A horizontal black line represents one family by connecting the repeating earthquake (red dots). The green and black curves are the normalized cumulative number of repeaters and ValEqt earthquakes respectively. (b) Normalized cumulative slip estimated from repeating earthquakes. (c) Times and magnitudes of ValEqt earthquakes (black dot) and repeating earthquakes (red dot). The blue star indicates the mainshock. (d, e and f) Same as (a, b and c) but zoomed in the vicinity of the mainshock time. Note that the normalized cumulative count of repeaters and ValEqt earthquakes starts at t=-2 days in (d).

figures/Main/repeaters_map.pdf

Figure 6. Space and time evolution of the ValEqt seismicity (black dot) and its repeating earthquakes (red dot). The blue star indicates the mainshock. a) Horizontal distribution of the seismicity. b) Latitudes, longitudes and magnitudes against the chronological index of the ValEqt seismicity. The chronological index in shown by the bottom horizontal axis ticks for each subplot. The corresponding time (days from mainshock) is shown with the top horizontal axis ticks. The two vertical dotted lines highlight the index/time of the first foreshock and the index/time of the mainshock, respectively.

The repeater activity is confined to a small region compared to the earthquakes in the ValEqt catalog (Figure 6). The main repeater activity is located in the vicinity of the mainshock hypocenter and a secondary activity is observed to the south before and after the largest aftershock. During the foreshock sequence, the repeater activity and the seismicity are almost perfectly co-located. After the mainshock, the repeater activity remains exclusively located at the initial foreshock location, unlike the seismicity that spreads to a wider area.

The aforementioned observations indicate that the repeater activity does not behave as a simple subset of the seismicity. Repeaters seem to be driven by an independent process that initiates before the mainshock within a specific area delimited by the foreshock activity. This recalls the occurrence of the preseismic aseismic transient slip (Ruiz et al., 2017; Caballero et al., 2021). We estimate the time-evolution of aseismic slip on the subduction interface from the observed repeater activity. We follow the approach of Kato et al. (2012, 2016) using a circular crack model with a constant stress drop of 3 MPa to estimate the individual repeater slip amplitudes (Hanks & Bakun, 2002; Uchida, 2019). Individual slip offsets are summed over time and averaged by the number of repeater families to estimate cumulative slip evolution (Figure 5). The obtained slip rate is maximum at the beginning of the foreshock sequence and slowly decays with time over days to months until the end of the studied time-period, although, as for the repeaters rate, the slip rate is slightly impacted by the occurrence of large earthquake.

5 Aseismic slip before and after the mainshock captured by high-rate GPS

Both the inferred unusual seismicity activity (Figure 2, 4) and the repeater-based slip rate (Figure 5, 6) suggest the presence of a specific triggering process before and after the mainshock, which is likely an aseismic slip. Indeed, the aseismic slip is reported for the pre-mainshock stage (Ruiz et al., 2017; Caballero et al., 2021), but temporal relationship between the aseismic preslip and the foreshock sequence remained unclear, which is key to understanding mechanical processes. For the post-mainshock stage, no studies have yet investigated very early postseismic deformation and rapid afterslip associated with the 2017 Valparaiso mainshock. Therefore, to fill the gap between the two stages, we use high-rate GPS (hereafter, HRGPS) to investigate transient slip during the whole 2017 sequence as independent observable from the seismicity analysis.

We employ 5-minute coordinates between 30 days before and after the mainshock at 6 sites near the epicenter (Figure S4) (Caballero et al., 2021), processed by Nevada Geodetic Laboratory (Blewitt et al., 2018). Nominal errors of these coordinates are $\sim$ 7 mm and $\sim$ 9 mm for east and north components, respectively. We do not use sites VALN and CUVI (Figure S4) because 5-min coordinates of the former are too noisy and those of the latter are not available. The original coordinates are affected by a high noise level, so we post-process the series to alleviate the fluctuations (Figure S5). We first fix the coordinates into the South American plate reference frame by using its Euler pole with respect to ITRF2014 (Altamimi et al., 2017) (black dots in Figure S5). Then, we remove the fluctuations associated with multipath (i.e., Choi et al., 2004; Itoh & Aoki, 2022; Larson et al., 2007; Ragheb et al., 2007), which is estimated as a seasonal component of "Seasonal-Trend decomposition using LOESS (STL)" (Cleveland et al., 1990; Pedregosa et al., 2011) with a period of 86100 seconds. This period is the closest integer multiple of the sampling interval to a typical repeat period of multipath signature (86154 seconds; Ragheb et al., 2007). Then, the multipath free time series (red in Figure S5) is corrected from a diurnal variation component following the same procedure as the multipath removal but with a repeat period of 86400 seconds in order to obtain diurnal fluctuations free series (purple in Figure S5).

Next, we remove the common mode fluctuation at all the sites, which are primarily due to fluctuation of reference frame and uncertainty of satellite orbits (e.g., Wdowinski et al., 1997). We extract common mode fluctuation (orange in Figure S5) by stacking coordinate time series at distant sites from the source area (Figure S4). Prior to stacking, we remove some outliers and the linear trend. Here, outliers are defined as epochs satisfying Equation 14 (Itoh et al., 2022).

$$\left| x_i - \frac{q_1 + q_3}{2} \right| > n * \frac{q_3 - q_1}{2} \tag{14}$$

where, x_i is displacement at the i-th epoch, q_1 and q_3 are the 25 and 75 percentile values of the position time series, respectively, and n is a threshold which was set to 8 in this study. The linear trend is estimated from the time series without outliers. The extracted common mode fluctuation is subsequently subtracted from the time series at the 6 sites of interest (blue in Figure S5).

Then, we remove the pre-mainshock trend from the common mode free time series. The linear trend is estimated from the data between 30 and 10 days before the mainshock. The trend is extrapolated to the subsequent period. Finally, we stack the cleaned time series at BN05 and TRPD, which are only $\sim$ 5 km apart, to further reduce the noise level (Figures S6 and S7). For stacking, the two time series are weighted according to the inverse of the square of quartile deviation of time series from 30 to 10 days before the mainshock. Hereafter, we assign a pseudo-name of site STAC to the stacked time series for the ease of writing and discussion.

The stacked time series at STAC, closest to the mainshock epicenter, clearly exhibits a westward transient motion before, during, and after the mainshock (Figure 7). The pre-mainshock transient motion started $\sim$3 days before the mainshock and $\sim$1 day before the largest foreshock (Figure 2). No acceleration of displacements is discernible before the mainshock, which can be interpreted as no acceleration of aseismic slip toward figures/Main/QTAY_STAC_east.pdf

Figure 7. Comparison of high-rate GPS displacements and seismicity evolution before and after the 2017 Valparaiso mainshock. a) Red dots indicate cleaned east positions between 5 days before and after the mainshock at the two closest sites QTAY and STAC (location shown in c)). Note that STAC is a pseudo-site name assigned to stacked time series of TRPD and BN05 (See text and Figure S4 for details). Black dots at the bottom panel indicate magnitude of detected seismicity. Notable large earthquakes are marked with stars, epicenters of which are shown in c). b) Same as a) but with data between 30 days before and after the mainshock. A moving median with a window length of 24 hours is shown in blue for each site. c) Site location (red inverted triangles) and epicenters (stars with corresponding colors with a) and b)). The same figure but for all available HRGPS sites is shown in Figure S6 for east displacement and S7 for north displacement.

the mainshock. Coseismic displacement associated with the largest foreshock is not resolved and possibly buried in the remaining noise given the expected amplitude of coseismic displacement (Caballero et al., 2021). Following the mainshock, very rapid postseismic deformation took place over ~1 day with an amplitude equal to ~25% of the mainshock coseismic displacement, followed by a slower but continuing deformation lasting until at least ~20 days with a displacement reaching ~50% of the mainshock coseismic one. This amount of postseismic displacement is, if interpreted as a proxy of afterslip moment, much larger than the global average of postseismic to coseismic slip moment ratio for $M > 6$ earthquakes (~30%) (Alwahedi & Hawthorne, 2019). Similarly, transient westward motion before and after the mainshock is visible with smaller amplitudes at QTAY, ~20 km south of STAC (Figure 7). At the other 3 sites, namely, CTPC, RCSD, and ROB1, the transient motion before the mainshock is less convincing whereas the postseismic transient motion following the mainshock are discernible. This postseismic motion pattern is not uniform, so it does not represent local artifacts (Figure S6). The north component of GPS coordinate time series does not exhibit discernible pre-mainshock motion but post-mainshock motion is visible at CTPC, RCSD, and ROB1 (Figure S7). Based on these predominantly trenchward motions, we conclude that the HRGPS observations before and after the mainshock indicate the presence of an aseismic slip along the megathrust at different rates.

6 Discussion and conclusion

In this study, we have investigated the seismic and aseismic processes during the 2017 Valparaiso seismic sequence, from the foreshocks to the post-seismic sequence. For that, we have first built a high resolution catalog of the seismicity from 2016 to 2021, improving the of completeness by 1 magnitude unit compared to the local CSN catalog. Thanks to this catalog, we have tested whether the seismicity can be explained by a stationary background term (describing a constant tectonic loading) and earthquake interactions. Two different temporal magnitude-dependent aftershock triggering models (i.e., ETASI and MISD models) have shown that the seismicity from the foreshock sequence up to several days after the mainshock (5 and 8 days, respectively) is more abundant than predicted. This result requires an additional forcing which may be linked to an increase of the slip rate on the interface. Such forcing had already been suggested by previous studies during the pre-seismic period (Ruiz et al., 2017; Caballero et al., 2021) but so far no study have investigated the processes taking place during the early post-seismic period, where the seismicity excess is persisting according to our analysis. To better document a potential increased slip rate on the interface, we have used both repeating earthquake and HRGPS positions during the entire sequence, including during the days following the mainshock. Assuming that the repeater rate is directly linked to the slip rate, our results indicate that a transient perturbation of the slip rate begins with the start of the foreshock sequence and then slowly decays over days to months without a clear termination. The steady evolution of the estimated slip rate indicates that the mainshock and large earthquakes have limited impacts on its time-evolution. Using HRGPS data, we have confirmed previous the geodetic observations of a slow slip during the foreshock sequence and clearly shown that it started ∼1 day before the occurrence of the first foreshock. The HRGPS time-series show a complex time-evolution after the mainshock: an immediate rapid westward displacement for ∼1 day, followed by a slower westward displacement gradually decelerating over a period of more than 20 days. This long-term westward displacement observed from before the foreshock sequence and up to several days after the mainshock is in first order consistent with the slip rate inferred from repeaters, and supports that the slow slip persists after the mainshock. Furthermore, both repeaters and HRGPS show no evidence of slip acceleration prior to the mainshock, suggesting that aseismic slip evolves independently of the mainshock.

All the analyzed signals do not perfectly agree with each other and indicate different start and end times of the identified transient. Setting the mainshock time as $t = 0$, the seismicity excess is evidenced from -1.5 to 5 days for the ETAS analysis and from -2 to 8 days for the MISD analysis. The repeating earthquakes track the slow slip event since the occurrence time of first foreshock (-2 days) up to months after the mainshock while the HRGPS suggests that the aseismic slip initiates ∼ 1 day before the first foreshock and persists at least for 20 days after the mainshock. Such differences reflect that these various observations are not sensitive to the same fault processes. Our land-based geodetic measurements reflect any slip along a large area of the subduction interface. On the other hand, the statistical seismicity analysis is representative of the process taking place only at the earthquake location. Finally, repeating earthquakes provide localized, but sparse in-situ measurements of the slip rate on a limited area of the interface (Figure 6). Defining the exact interplay between all of these observations is challenging, but we may consider that they are broadly interconnected because of their similar timing extending from the foreshock sequence up to post-mainshock times.

The differences of slip behavior inferred from different observations may also partly result from uncertainties and hypotheses inherent to our analysis approach. As earthquakes actually interact in space, the ETAS and MISD models are often used with a spatial kernel to weight inter-event distances in the aftershock triggering scheme (Zhuang et al., 2011). However, in this study, we focus only on the temporal variations of seismicity, as spatial considerations would likely complicate the aftershock triggering association in such a small study area. Because of the location uncertainties of earthquakes due to the geometry of our network, the apparent inter-event distance is not well constrained and may lead to unrealistic event association. Yet, thanks to our careful spatial selection, we believe that the ValEqt seismicity is sufficiently isolated and uniquely clustered around the mainshock to be analyzed temporally (see Section 2; Figure 1). We acknowledge that the repeating earthquake detection and the inferred slip rate is prone to multiple uncertainties. First, the repeating earthquake detection is also impacted by the rate dependent incompleteness mentioned in Section 3. As we cannot detect a lot of low magnitude earthquakes when the seismicity rate is high, we also miss possible repeaters. Such incompleteness may impact the slip rate inferred just after the mainshock and other large earthquakes. Moreover, when the seismicity rate is high, the 40 second cross-correlation window is likely to screen several successive waveforms and further blur the detection of potential repeaters. To evaluate the influence of the window length, we also performed the repeater detection using a smaller cross-correlation windows centered only on the P phases. Because the window is shorter, we obtained more repeaters families for the same CC threshold, but with similar conclusions as the ones presented here (see Figure S8). Second, the repeater rupture sizes and slips is estimated with standard scaling laws and apriori values (i.e., stress-drop, shear modulus). Using different scaling law or stress drop (Uchida, 2019; Nadeau & Johnson, 1998; Hanks & Bakun, 2002) yielded slightly different repeater families and absolute slip estimates, but still we can draw similar conclusions (see Table S1 and Figure S9). In order to minimize the influence of such choice on the absolute amount of slip observed, we focus only on its temporal evolution pattern. The HRGPS data contains plenty of noise inherent to the processing strategy, which were not completely removed in this study. The remaining noise limits the possibility to capture second order features of the slab interface processes, such as an accelerated slip just before the mainshock. Moreover, our HRGPS displacements can contain significant seismic slip contributions (e.g., Caballero et al., 2021) although we assumed that our HRGPS displacements predominantly represent the contribution from aseismic slip in this study. From this viewpoint, seismic deformation produced by the post-mainshock bursts identified by our ETASI analysis probably alleviates the discrepancy between the HRGPS-based very rapid afterslip and the repeater-based steady aseismic slip evolution. Nevertheless, quantification of displacements associated with the post-mainshock bursts is beyond the scope of this study.

In spite of these limitations, our observations bring new insight on the possible mechanisms that have driven the 2017 Valparaiso seismic sequence. As previously mentioned, precursory slow slip is often interpreted as the nucleation phase slowly accelerating toward the mainshock dynamic rupture (Das & Scholz, 1981; Dieterich, 1992; Ampuero & Rubin, 2008; Ohnaka, 1992; Latour et al., 2013). In this model, monitoring foreshocks (small asperities loaded by the slipping interface) and the aseismic slip may help to track the ongoing rupture and carry a strong predictive power on the subsequent mainshock occurrence. In the 2017 Valparaiso case, however, there is no evidence of acceleration of slip leading up to the mainshock and both the seismicity excess and the aseismic slip persist after the mainshock. Therefore, we believe that the seismic and aseismic processes observed before and after the Valparaiso mainshock cannot be interpreted as a (accelerating) pre-slip nucleation phase. Rather, a model described by Meng and Duan (2022) can be a better alternative. In this model, the slow slip event evolves independently from the mainshock dynamic rupture, only acting as an aseismic loading of nearby asperities. The ongoing slow slip event triggers seismicity by breaking embedded small asperities, which may further enhance the rupture of nearby areas with usual earthquake interactions. Within such a slow-slip enhanced seismicity, the probability to observe a large earthquake (i.e., a mainshock) is increased but is not deterministic as for the nucleation phase model. The aseismic loading framework can explain the persistence of the enhanced seismicity and the aseismic slip after the Valparaiso mainshock and the lack of observed slip acceleration before it. Similar observations of a continuously enhanced foreshock and post-mainshock seismicity have been previously reported by Marsan et al. (2014). They showed that worldwide mainshocks preceded by an enhanced foreshock seismicity are also associated with an enhanced aftershock activity. They suggest that such observation likely requires external triggering process such as aseismic slip or/and fluid migrations that occur before and after the mainshock occurrence. Large earthquakes triggered by independent aseismic loading processes have already been observed in other regions that are frequently associated with slow slip events. As previously mentioned, Radiguet et al. (2016) showed that recurrent slow-slips with no mainshock have been observed on the same interface for years, before finally triggering the 2014 $M_w = 7.3$ Papanoa earthquake. Similar recurrent slow-slip observations were associated with the triggering of the 2012 $M_w = 7.6$ earthquake in Costa Rica (Voss et al., 2018) or the 2020 $M_w = 6.9$ mainshock in the Atacama region in Chile (Klein et al., 2018, 2021, 2023), that was followed with unusually large post-seismic displacements. There are also numerous examples of slow slip events that have been associated with seismicity swarms but not followed by a large mainshock (Lohman & McGuire, 2007; Vallée et al., 2013; Nishikawa et al., 2021). All of these observations suggest that mainshocks preceded by both an aseismic slip and an enhanced foreshock activity may simply be a probabilistic occurrence of a large rupture included in a continuous enhanced seismicity regime, mediated by a long-term underlying process.

Therefore, to properly address the precursory nature of unusual aseismic and seismic activities, earthquake sequences needs to be continuously analyzed from the foreshock to the post-mainshock activity. Finally, although this model is not as deterministic as the nucleation phase model, the real-time monitoring of aseismic slip and enhanced seismicity can provide useful additional information about the state of seismic hazard on an aseismically slipping fault.

7 Open Research

Broadband seismological data are provided by the National Seismological Center (CSN) of the University of Chile through the Incorporated Research Institutions for Seismology Data Management Center (IRIS-DMC) under networks C1.

The High rate GPS positions provided by Nevada Geodetic Laboratory, University of Nevada, Reno are available at `http://geodesy.unr.edu/`.

Our catalog of earthquakes and repeating earthquakes (Moutote et al., 2023) can be found at : https://doi.org/10.5281/zenodo.7665026

Phase picking software EQTransformer (Mousavi et al., 2020b) can be found at : https://github.com/smousavi05/EQTransformer

Phase association software REAL (Zhang et al., 2019b) can be found at : https://github.com/Dalmzhang/REAL

The location software NonLinLoc (Lomax, 2017) can be found at : http://alomax.free.fr/nlloc/

The double difference relocation software HypoDD (Waldhauser & Ellsworth, 2010) can be found at : https://www.ldeo.columbia.edu/~felixw/hypoDD.html

Acknowledgments

Discussion with Mathilde Radiguet for HRGPS post-processing was fruitful. This work was supported by the European Research Council (ERC) (under the European Union's Horizon 2020 research and innovation program under grant agreement No. 805256 and No. 865963). Y.I. is an Overseas Research Fellow of the Japan Society of the Promotion of Science.

References

Altamimi, Z., Métivier, L., Rebischung, P., Rouby, H., & Collilieux, X. (2017). ITRF2014 plate motion model. *Geophysical Journal International*, *209*(3), 1906-1912. doi: 10.1093/gji/ggx136

Alwahedi, M. A., & Hawthorne, J. C. (2019). Intermediate-magnitude postseismic slip follows intermediate-magnitude (m 4 to 5) earthquakes in california. *Geophysical Research Letters*, *46*(7), 3676-3687. doi: https://doi.org/10.1029/2018GL081001

Ampuero, J.-P., & Rubin, A. M. (2008). Earthquake nucleation on rate and state faults – Aging and slip laws. *Journal of Geophysical Research: Solid Earth*, *113*(B1). doi: 10.1029/2007JB005082

Barrientos, S., & National Seismological Center (CSN) Team. (2018). The Seismic Network of Chile. *Seismological Research Letters*, *89*(2A), 467–474. doi: 10.1785/0220160195

Blewitt, G., Hammond, W. C., & Kreemer, C. (2018). Harnessing the gps data explosion for interdisciplinary science. *EOS*, *99*. doi: 10.1029/2018EO104623

Bouchon, M., Durand, V., Marsan, D., Karabulut, H., & Schmittbuhl, J. (2013). The long precursory phase of most large interplate earthquakes. *Nature Geoscience*, *6*(4), 299–302. doi: 10.1038/ngeo1770

Bouchon, M., Karabulut, H., Aktar, M., Özalaybey, S., Schmittbuhl, J., & Bouin, M.-P. (2011). Extended nucleation of the 1999 mw 7.6 izmit Earthquake. *Science*, *331*(6019), 877–880. doi: 10.1126/science.1197341

Brodsky, E. E., & Lay, T. (2014). Recognizing Foreshocks from the 1 April 2014 Chile Earthquake. *Science*, *344*(6185), 700–702. doi: 10.1126/science.1255202

Caballero, E., Chounet, A., Duputel, Z., Jara, J., Twardzik, C., & Jolivet, R. (2021). Seismic and aseismic fault slip during the initiation phase of the 2017 $m_w = 6.9$ valparaíso earthquake. *Geophysical Research Letters*, *48*(6). doi: 10.1029/2020GL091916

Choi, K., Bilich, A., Larson, K. M., & Axelrad, P. (2004). Modified sidereal filtering: Implications for high-rate gps positioning. *Geophysical Research Letters*, *31*(22). doi: 10.1029/2004GL021621

Cleveland, R. B., Cleveland, W. S., McRae, J. E., & Terpenning, I. (1990). Stl: A seasonal-trend decomposition. *J. Off. Stat*, *6*(1), 3–73.

Das, S., & Scholz, C. H. (1981). Theory of time-dependent rupture in the Earth. *Journal of Geophysical Research: Solid Earth*, *86*(B7), 6039–6051. doi: 10.1029/JB086iB07p06039

Davidsen, J., & Baiesi, M. (2016). Self-similar aftershock rates. *Physical Review E*, *94*(2). doi: 10.1103/PhysRevE.94.022314

de Arcangelis, L., Godano, C., & Lippiello, E. (2018). The overlap of aftershock coda waves and Short-Term postseismic forecasting. *Journal of Geophysical Research: Solid Earth*, *123*(7), 5661–5674. doi: 10.1029/2018JB015518

Dieterich, J. H. (1992). Earthquake nucleation on faults with rate-and state-dependent strength. *Tectonophysics*, *211*(1), 115–134. doi: 10.1016/0040-1951(92)90055-B

Dodge, D. A., Beroza, G. C., & Ellsworth, W. L. (1995). Foreshock sequence of the 1992 Landers, California, earthquake and its implications for earthquake nucleation. *Journal of Geophysical Research: Solid Earth*, *100*(B6), 9865–9880. doi: 10.1029/95JB00871

Dodge, D. A., Beroza, G. C., & Ellsworth, W. L. (1996). Detailed observations of California foreshock sequences: Implications for the earthquake initiation process. *Journal of Geophysical Research: Solid Earth*, *101*(B10), 22371–22392. doi: 10.1029/96JB02269

Ellsworth, W. L., & Bulut, F. (2018). Nucleation of the 1999 Izmit earthquake by a triggered cascade of foreshocks. *Nature Geosci*, *11*(7), 531–535. doi: 10.1038/s41561-018-0145-1

Felzer, K. R., Abercrombie, R. E., & Ekström, G. (2004). A Common Origin for Aftershocks, Foreshocks, and Multiplets. *Bulletin of the Seismological Society of America*, *94*(1), 88–98. doi: 10.1785/0120030069

Gomberg, J. (2018). Unsettled earthquake nucleation. *Nature Geoscience*, *11*(7), 463–464. doi: 10.1038/s41561-018-0149-x

Hainzl, S. (2016). Apparent triggering function of aftershocks resulting from rate-dependent incompleteness of earthquake catalogs. *Journal of Geophysical Research: Solid Earth*, *121*(9), 6499–6509. doi: 10.1002/2016JB013319

Hainzl, S. (2021). ETAS-Approach Accounting for Short-Term Incompleteness of Earthquake Catalogs. *Bulletin of the Seismological Society of America*. doi: 10.1785/0120210146

Hanks, T. C., & Bakun, W. H. (2002). A Bilinear Source-Scaling Model for M-log A Observations of Continental Earthquakes. *Bulletin of the Seismological Society of America*, *92*(5), 1841–1846. doi: 10.1785/0120010148

Helmstetter, A., & Sornette, D. (2003). Foreshocks explained by cascades of triggered seismicity. *Journal of Geophysical Research: Solid Earth*, *108*(B10). doi: 10.1029/2003JB002409

Igarashi, T., Matsuzawa, T., & Hasegawa, A. (2003). Repeating earthquakes and interplate aseismic slip in the northeastern Japan subduction zone. *Journal of Geophysical Research: Solid Earth*, *108*(B5). doi: 10.1029/2002JB001920

Itoh, Y., & Aoki, Y. (2022). On the performance of position-domain sidereal filter for 30-s kinematic gps to mitigate multipath errors. *Earth, Planets and Space*, *74*(1), 1–20. doi: 10.1186/s40623-022-01584-8

Itoh, Y., Aoki, Y., & Fukuda, J. (2022). Imaging evolution of cascadia slow-slip event using high-rate gps. *Scientific reports*, *12*(1), 1–12. doi: 10.1038/s41598-022-10957-8

Kagan, Y. Y. (2004). Short-Term properties of earthquake catalogs and models of earthquake source. *Bulletin of the Seismological Society of America*, *94*(4), 1207–1228. doi: 10.1785/012003098

Kaneko, Y., & Ampuero, J.-P. (2011). A mechanism for preseismic steady rupture fronts observed in laboratory experiments. *Geophysical Research Letters*, *38*(21). doi: 10.1029/2011GL049953

Kato, A., Fukuda, J., Kumazawa, T., & Nakagawa, S. (2016). Accelerated nucleation of the 2014 Iquique, Chile Mw 8.2 Earthquake. *Sci Rep*, *6*(1), 24792. doi: 10.1038/srep24792

Kato, A., Obara, K., Igarashi, T., Tsuruoka, H., Nakagawa, S., & Hirata, N. (2012). Propagation of Slow Slip Leading Up to the 2011 Mw 9.0 Tohoku-Oki Earthquake. *Science*, *335*(6069), 705–708. doi: 10.1126/science.1215141

Klein, E., Duputel, Z., Zigone, D., Vigny, C., Boy, J.-P., Doubre, C., & Meneses, G. (2018). Deep Transient Slow Slip Detected by Survey GPS in the Region of Atacama, Chile. *Geophysical Research Letters*, *45*(22), 12,263–12,273. doi: 10.1029/2018GL080613

Klein, E., Potin, B., Pasten-Araya, F., Tissandier, R., Azua, K., Duputel, Z., ... Vigny, C. (2021). Interplay of seismic and a-seismic deformation during the 2020 sequence of Atacama, Chile. *Earth and Planetary Science Letters*, *570*, 117081. doi: 10.1016/j.epsl.2021.117081

Klein, E., Vigny, C., Duputel, Z., Zigone, D., Rivera, L., Ruiz, S., & Potin, B. (2023). Return of the Atacama deep Slow Slip Event: The 5-year recurrence confirmed by continuous GPS. *Physics of the Earth and Planetary Interiors*, *334*, 106970. doi: 10.1016/j.pepi.2022.106970

Larson, K. M., Bilich, A., & Axelrad, P. (2007). Improving the precision of high-rate gps. *Journal of Geophysical Research: Solid Earth*, *112*(B5). doi: 10.1029/2006JB004367

Latour, S., Schubnel, A., Nielsen, S., Madariaga, R., & Vinciguerra, S. (2013). Characterization of nucleation during laboratory earthquakes. *Geophys. Res. Lett.*, *40*(19), 5064–5069. doi: 10.1002/grl.50974

Llenos, A. L., McGuire, J. J., & Ogata, Y. (2009). Modeling seismic swarms triggered by aseismic transients. *Earth and Planetary Science Letters*, *281*(1), 59–69. doi: 10.1016/j.epsl.2009.02.011

Lohman, R. B., & McGuire, J. J. (2007). Earthquake swarms driven by aseismic creep in the Salton Trough, California. *Journal of Geophysical Research: Solid Earth*, *112*(B4). doi: 10.1029/2006JB004596

Lomax, A. (2017). *NonLinLoc 7.0* [software]. Retrieved from `http://alomax.free.fr/nlloc/`

Lomax, A., Virieux, J., Volant, P., & Berge-Thierry, C. (2000). Probabilistic Earthquake Location in 3D and Layered Models. In G. Nolet, C. H. Thurber, & N. Rabinowitz (Eds.), *Advances in Seismic Event Location* (Vol. 18, pp. 101–134). Dordrecht. doi: 10.1007/978-94-015-9536-0_5

Marill, L., Marsan, D., Socquet, A., Radiguet, M., Cotte, N., & Rousset, B. (2021). Fourteen-Year Acceleration Along the Japan Trench. *Journal of Geophysical Research: Solid Earth*, *126*(11), e2020JB021226. doi: 10.1029/2020JB021226

Marsan, D., & Enescu, B. (2012). Modeling the foreshock sequence prior to the 2011, MW9.0 Tohoku, Japan, earthquake. *Journal of Geophysical Research: Solid Earth*, *117*(B6). doi: 10.1029/2011JB009039

Marsan, D., Helmstetter, A., Bouchon, M., & Dublanchet, P. (2014). Foreshock activity related to enhanced aftershock production: Foreshock and aftershock activities. *Geophysical Research Letters*, *41*(19), 6652–6658. doi: 10.1002/2014GL061219

Marsan, D., & Lengline, O. (2008). Extending earthquakes' reach through cascading. *Science*, *319*(5866), 1076–1079.

Marsan, D., & Lengliné, O. (2010). A new estimation of the decay of aftershock density with distance to the mainshock. *Journal of Geophysical Research: Solid Earth*, *115*(B9).

Mavrommatis, A. P., Segall, P., & Johnson, K. M. (2014). A decadal-scale deformation transient prior to the 2011 Mw 9.0 Tohoku-oki earthquake. *Geophys. Res. Lett.*, *41*(13), 4486–4494. doi: 10.1002/2014GL060139

Mavrommatis, A. P., Segall, P., Uchida, N., & Johnson, K. M. (2015). Long-term acceleration of aseismic slip preceding the Mw 9 Tohoku-oki earthquake: Constraints from repeating earthquakes. *Geophysical Research Letters*, *42*(22), 9717–9725. doi: 10.1002/2015GL066069

McLaskey, G. C. (2019). Earthquake Initiation From Laboratory Observations and Implications for Foreshocks. *Journal of Geophysical Research: Solid Earth*, *124*(12), 12882–12904. doi: 10.1029/2019JB018363

Meng, Q., & Duan, B. (2022). Dynamic Modeling of Interactions between Shallow Slow-Slip Events and Subduction Earthquakes. *Seismological Research Letters*. doi: 10.1785/0220220138

Mignan, A. (2015). The debate on the prognostic value of earthquake foreshocks: A meta-analysis. *Scientific Reports*, *4*(1), 4099. doi: 10.1038/srep04099

Mousavi, S. M., Ellsworth, W. L., Zhu, W., Chuang, L. Y., & Beroza, G. C. (2020a). Earthquake transformer—an attentive deep-learning model for simultaneous earthquake detection and phase picking. *Nature Communications*, *11*(1), 3952. doi: 10.1038/s41467-020-17591-w

Mousavi, S. M., Ellsworth, W. L., Zhu, W., Chuang, L. Y., & Beroza, G. C. (2020b). *EQTransformer* [software]. Retrieved from `https://github.com/smousavi05/EQTransformer`

Moutote, L., Lengliné, O., & Duputel, Z. (2023). *ValEqt: A high-resolution Earthquake and Repeating earthquakes catalog of the 2017 Valparaiso sequence* [dataset]. Zenodo. Retrieved from `https://doi.org/10.5281/zenodo.7665026` doi: 10.5281/zenodo.7665026

Moutote, L., Marsan, D., Lengliné, O., & Duputel, Z. (2021). Rare occurrences of non-cascading foreshock activity in Southern California. *Geophysical Research Letters*, *48*(7), e2020GL091757. doi: 10.1029/2020GL091757

Nadeau, R. M., & Johnson, L. R. (1998). Seismological studies at Parkfield VI: Moment release rates and estimates of source parameters for small repeating earthquakes. *Bulletin of the Seismological Society of America*, *88*(3), 790–814. doi: 10.1785/BSSA0880030790

Nishikawa, T., Nishimura, T., & Okada, Y. (2021). Earthquake Swarm Detection Along the Hikurangi Trench, New Zealand: Insights Into the Relationship Between Seismicity and Slow Slip Events. *Journal of Geophysical Research: Solid Earth*, *126*(4), e2020JB020618. doi: 10.1029/2020JB020618

Ogata, Y. (1988). Statistical Models for Earthquake Occurrences and Residual Analysis for Point Processes. *Journal of the American Statistical Association*, *83*(401), 9–27. doi: 10.1080/01621459.1988.10478560

Ogata, Y. (1989). Statistical model for standard seismicity and detection of anomalies by residual analysis. *Tectonophysics*, *169*(1-3), 159–174. doi: 10.1016/0040-1951(89)90191-1

Ogata, Y. (1992). Detection of precursory relative quiescence before great earthquakes through a statistical model. *Journal of Geophysical Research*, *97*(B13), 19845. doi: 10.1029/92JB00708

Ohnaka, M. (1992). Earthquake source nucleation: A physical model for short-term precursors. *Tectonophysics*, *211*(1), 149–178. doi: 10.1016/0040-1951(92)90057-D

Omori, F. (1895). On the After-shocks of Earthquakes. *The journal of the College of Science, Imperial University*, *7*(2), 111–200. doi: 10.15083/00037562

Pedregosa, F., Varoquaux, G., Gramfort, A., Michel, V., Thirion, B., Grisel, O., … others (2011). Scikit-learn: Machine learning in python. *the Journal of machine Learning research*, *12*, 2825–2830.

Peng, Z., Vidale, J. E., Ishii, M., & Helmstetter, A. (2007). Seismicity rate immediately before and after main shock rupture from high-frequency waveforms in japan. *Journal of Geophysical Research: Solid Earth*, *112*(B3).

Radiguet, M., Perfettini, H., Cotte, N., Gualandi, A., Valette, B., Kostoglodov, V., … Campillo, M. (2016). Triggering of the 2014 Mw7.3 Papanoa earthquake by a slow slip event in Guerrero, Mexico. *Nature Geoscience*, *9*(11), 829–833. doi: 10.1038/ngeo2817

Ragheb, A., Clarke, P. J., & Edwards, S. (2007). Gps sidereal filtering: coordinate- and carrier-phase-level strategies. *Journal of Geodesy*, *81*(5), 325–335. doi: 10.1007/s00190-006-0113-1

Richter, C. F. (1935). An instrumental earthquake magnitude scale. *Bulletin of the Seismological Society of America*, *25*(1), 2–32. doi: 10.1785/BSSA0250010001

Richter, C. F. (1958). *Elementary Seismology.*

Ross, Z. E., Trugman, D. T., Hauksson, E., & Shearer, P. M. (2019). Searching for hidden earthquakes in Southern California. *Science*, *364*(6442), 767–771. doi: 10.1126/science.aaw6888

Rubin, A. M., & Ampuero, J.-P. (2005). Earthquake nucleation on (aging) rate and state faults. *Journal of Geophysical Research: Solid Earth*, *110*(B11). doi: 10.1029/2005JB003686

Ruiz, S., Aden-Antoniow, F., Baez, J. C., Otarola, C., Potin, B., del Campo, F., … Bernard, P. (2017). Nucleation Phase and Dynamic Inversion of the Mw 6.9 Valparaíso 2017 Earthquake in Central Chile. *Geophys. Res. Lett.*, *44*(20), 10,290–10,297. doi: 10.1002/2017GL075675

Ruiz, S., Metois, M., Fuenzalida, A., Ruiz, J., Leyton, F., Grandin, R., … Campos, J. (2014). Intense foreshocks and a slow slip event preceded the 2014 Iquique Mw 8.1 earthquake. *Science*, *345*(6201), 1165–1169.

Seif, S., Zechar, J. D., Mignan, A., Nandan, S., & Wiemer, S. (2019). Foreshocks and their potential deviation from general seismicity. *Bulletin of the Seismolog-*

ical Society of America, *109*(1), 1–18. doi: 10.1785/0120170188

Shearer, P. M. (2019). *Introduction to Seismology* (3rd edition ed.). Cambridge ; New York, NY.

Socquet, A., Valdes, J. P., Jara, J., Cotton, F., Walpersdorf, A., Cotte, N., ... Norabuena, E. (2017). An 8 month slow slip event triggers progressive nucleation of the 2014 Chile megathrust. *Geophysical Research Letters*, *44*(9), 4046–4053. doi: 10.1002/2017GL073023

Tape, C., Holtkamp, S., Silwal, V., Hawthorne, J., Kaneko, Y., Ampuero, J. P., ... West, M. E. (2018). Earthquake nucleation and fault slip complexity in the lower crust of central Alaska. *Nature Geoscience*, *11*(7), 536–541. doi: 10.1038/s41561-018-0144-2

Taroni, M., Marzocchi, W., Schorlemmer, D., Werner, M. J., Wiemer, S., Zechar, J. D., ... Euchner, F. (2018). Prospective CSEP Evaluation of 1-Day, 3-Month, and 5-Yr Earthquake Forecasts for Italy. *Seismological Research Letters*, *89*(4), 1251–1261. doi: 10.1785/0220180031

Uchida, N. (2019). Detection of repeating earthquakes and their application in characterizing slow fault slip. *Progress in Earth and Planetary Science*, *6*(1), 40. doi: 10.1186/s40645-019-0284-z

Utsu, T., Ogata, Y., S, R., & Matsu'ura. (1995). The Centenary of the Omori Formula for a Decay Law of Aftershock Activity. *Journal of Physics of the Earth*, *43*(1), 1–33. doi: 10.4294/jpe1952.43.1

Vallée, M., Nocquet, J.-M., Battaglia, J., Font, Y., Segovia, M., Régnier, M., ... Chlieh, M. (2013). Intense interface seismicity triggered by a shallow slow slip event in the Central Ecuador subduction zone. *Journal of Geophysical Research: Solid Earth*, *118*(6), 2965–2981. doi: 10.1002/jgrb.50216

van den Ende, M. P. A., & Ampuero, J.-P. (2020). On the Statistical Significance of Foreshock Sequences in Southern California. *Geophys. Res. Lett.*, *47*(3). doi: 10.1029/2019GL086224

Voss, N., Dixon, T. H., Liu, Z., Malservisi, R., Protti, M., & Schwartz, S. (2018). Do slow slip events trigger large and great megathrust earthquakes? *Science Advances*, *4*(10), eaat8472. doi: 10.1126/sciadv.aat8472

Waldhauser, F., & Ellsworth, W. L. (2000). A Double-Difference Earthquake Location Algorithm: Method and Application to the Northern Hayward Fault, California. *Bulletin of the Seismological Society of America*, *90*(6), 1353–1368. doi: 10.1785/0120000006

Waldhauser, F., & Ellsworth, W. L. (2010). *HypoDD 1.3* [dataset]. Retrieved from `https://www.ldeo.columbia.edu/~felixw/hypoDD.html`

Wdowinski, S., Bock, Y., Zhang, J., Fang, P., & Genrich, J. (1997). Southern california permanent gps geodetic array: Spatial filtering of daily positions for estimating coseismic and postseismic displacements induced by the 1992 landers earthquake. *Journal of Geophysical Research: Solid Earth*, *102*(B8), 18057-18070. doi: 10.1029/97JB01378

Zhang, M., Ellsworth, W. L., & Beroza, G. C. (2019a). Rapid earthquake association and location. *Seismological Research Letters*, *90*(6), 2276–2284. doi: 10.1785/0220190052

Zhang, M., Ellsworth, W. L., & Beroza, G. C. (2019b). *REAL* [software]. Retrieved from `https://github.com/Dal-mzhang/REAL`

Zhuang, J. (2012). Long-term earthquake forecasts based on the epidemic-type aftershock sequence (ETAS) model for short-term clustering. *Research in Geophysics*, *2*(1), e8–e8. doi: 10.4081/rg.2012.e8

Zhuang, J., Harte, D., Werner, M. J., Hainzl, S., & Zhou, S. (2012). Basic models of seismicity: Temporal models. *Community Online Resource for Statistical Seismicity Analysis*, *Theme V*(1).

Zhuang, J., & Touati, S. (2015). Stochastic simulation of earthquake catalogs. *Community Online Resource for Statistical Seismicity Analysis*, *Theme V*(1), 34.

Zhuang, J., Werner, M. J., Hainzl, S., Harte, D., & Zhou, S. (2011). Basic models of seismicity: Spatiotemporal models. *Community Online Resource for Statistical Seismicity Analysis*, *Theme V*(1), 20.

Figure 1.

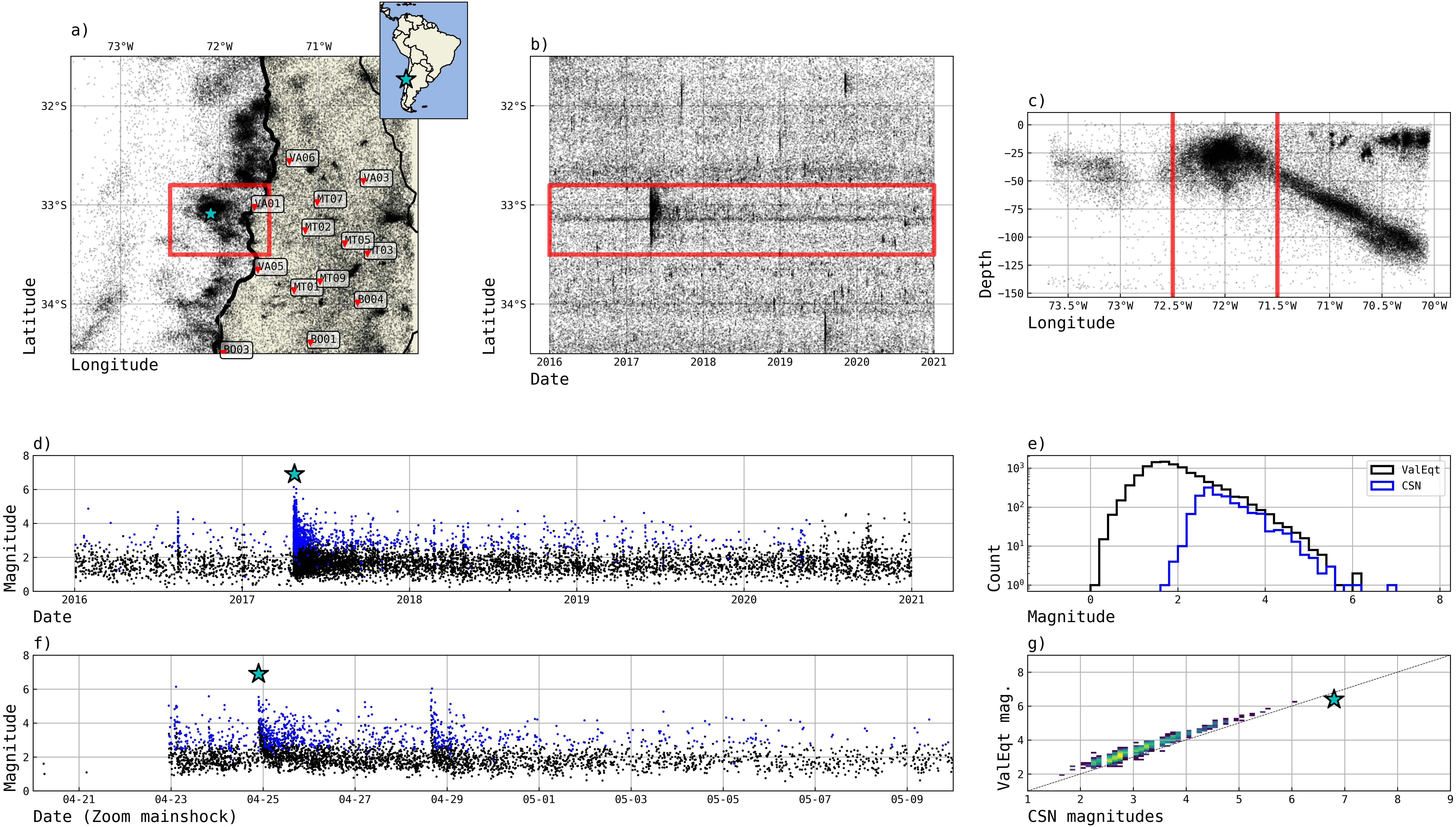

a)
73°W
72°W
71°W
32°S
33°S
34°S
VA06
VA03
VA01
MT07
MT02
MT05
MT03
VA05
MT09
MT01
B004
B001
B003
Latitude
Longitude
b)
32°S
33°S
34°S
2016
2017
2018
2019
2020
2021
Latitude
Date
c)
0
−25
−50
−75
−100
−125
−150
73.5°W
73°W
72.5°W
72°W
71.5°W
71°W
70.5°W
70°W
Depth
Longitude
d)
Magnitude
Date
e)
ValEqt
CSN
Count
Magnitude
f)
04-21
04-23
04-25
04-27
04-29
05-01
05-03
05-05
05-07
05-09
Magnitude
Date (Zoom mainshock)
g)
ValEqt mag.
CSN magnitudes

Figure 2.

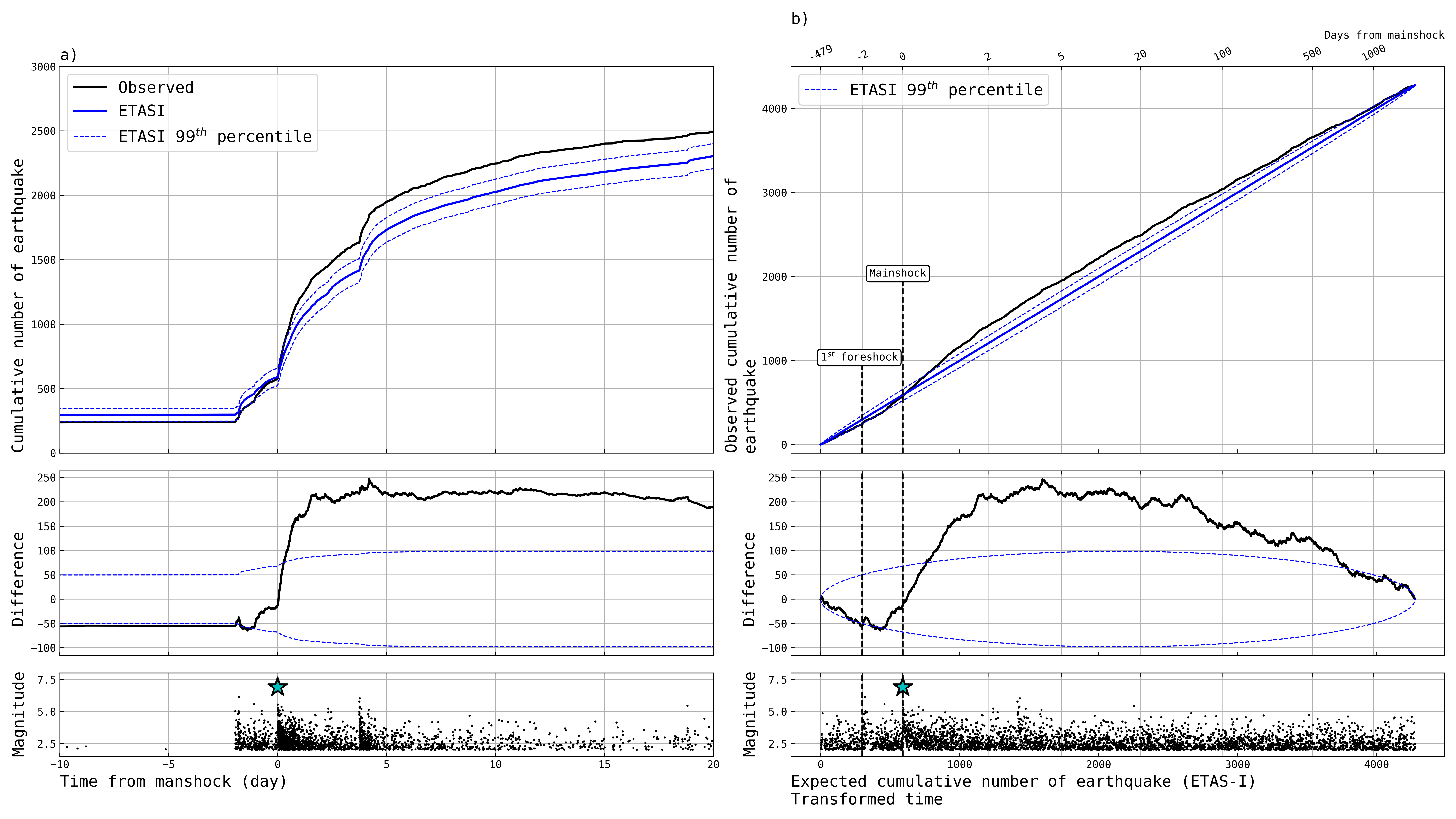

a)
b)
Observed
ETASI
ETASI 99th percentile
Cumulative number of earthquake
Difference
Magnitude
Time from manshock (day)
Days from mainshock
-479
-2
0
2
5
20
100
500
1000
Mainshock
1st foreshock
Observed cumulative number of earthquake
Expected cumulative number of earthquake (ETAS-I)
Transformed time

Figure 3.

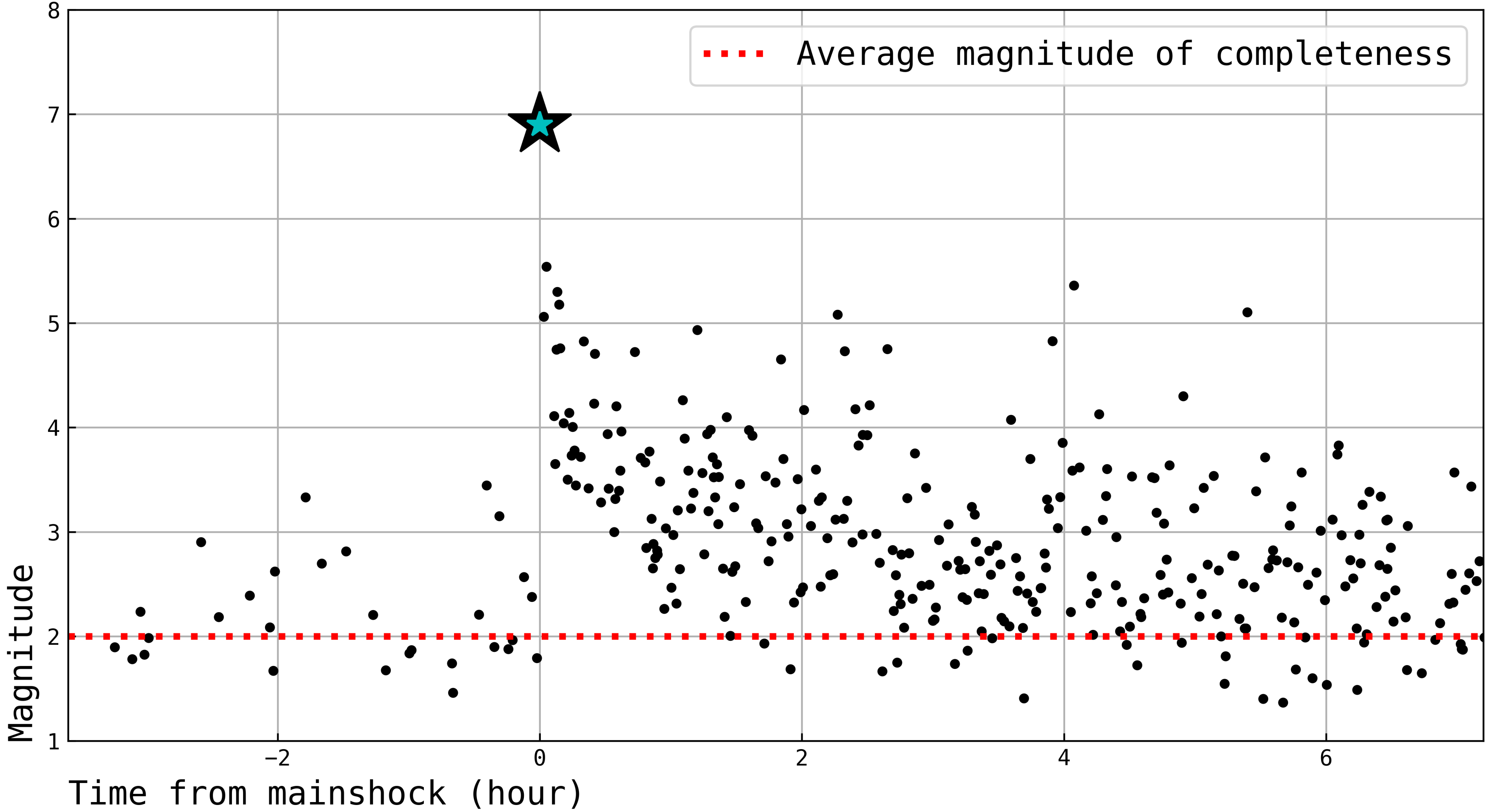

Average magnitude of completeness
Magnitude
Time from mainshock (hour)
8
7
6
5
4
3
2
1
−2
0
2
4
6

Figure 4.

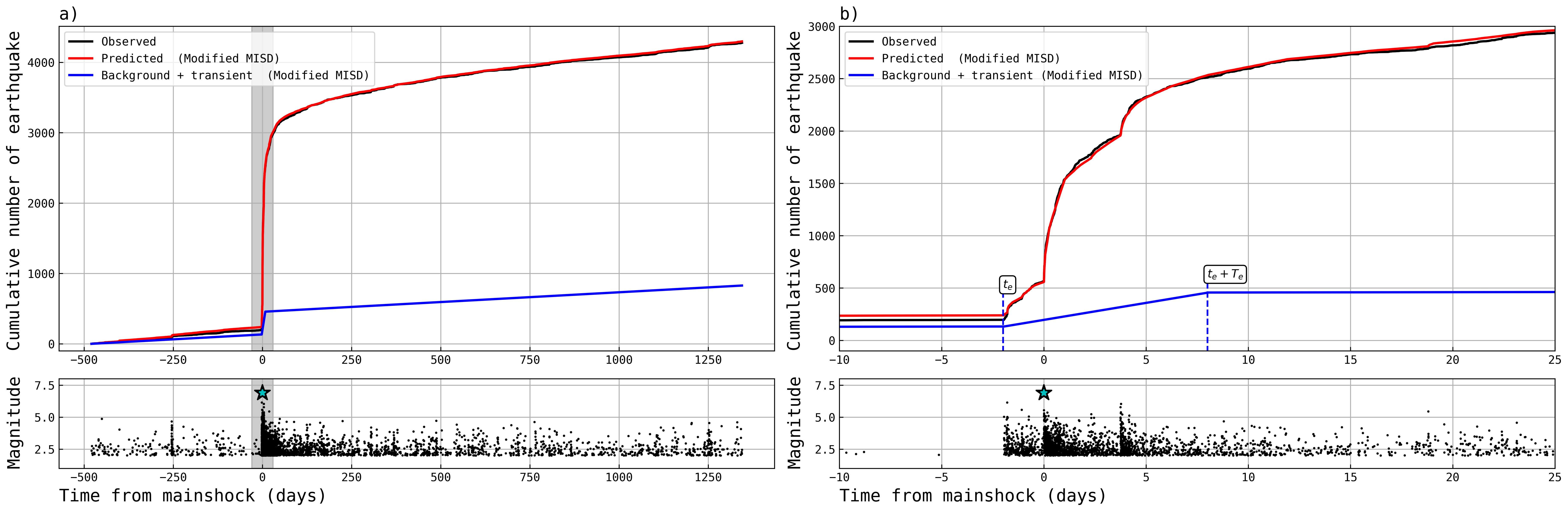
a)
b)
Observed
Predicted (Modified MISD)
Background + transient (Modified MISD)
Cumulative number of earthquake
Magnitude
Time from mainshock (days)
t_e
$t_e + T_e$

Figure 5.

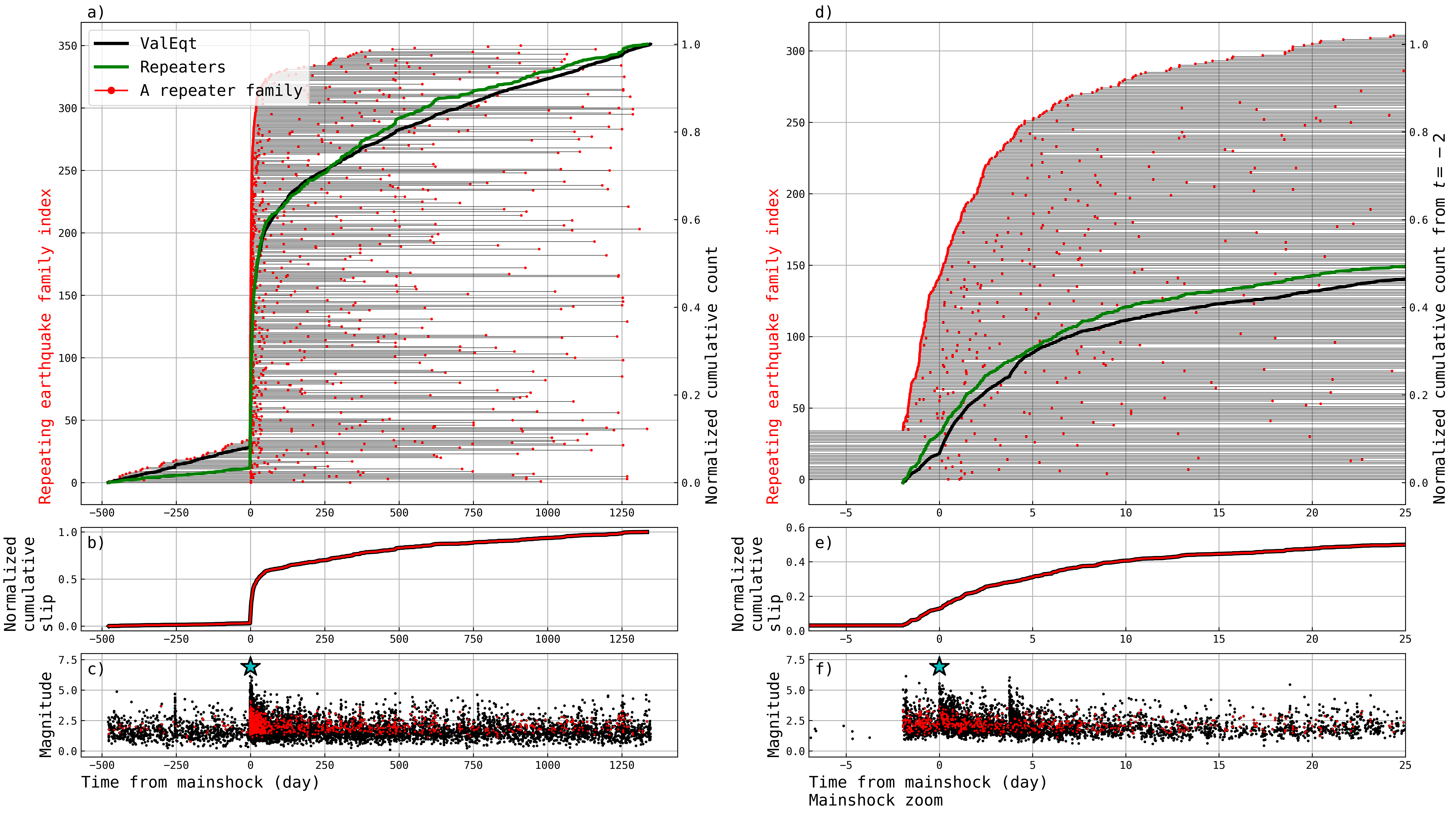

a)
ValEqt
Repeaters
A repeater family
Repeating earthquake family index
Normalized cumulative count
b)
Normalized cumulative slip
c)
Magnitude
Time from mainshock (day)
d)
Repeating earthquake family index
Normalized cumulative count from $t = -2$
e)
Normalized cumulative slip
f)
Magnitude
Time from mainshock (day)
Mainshock zoom

Figure 6.

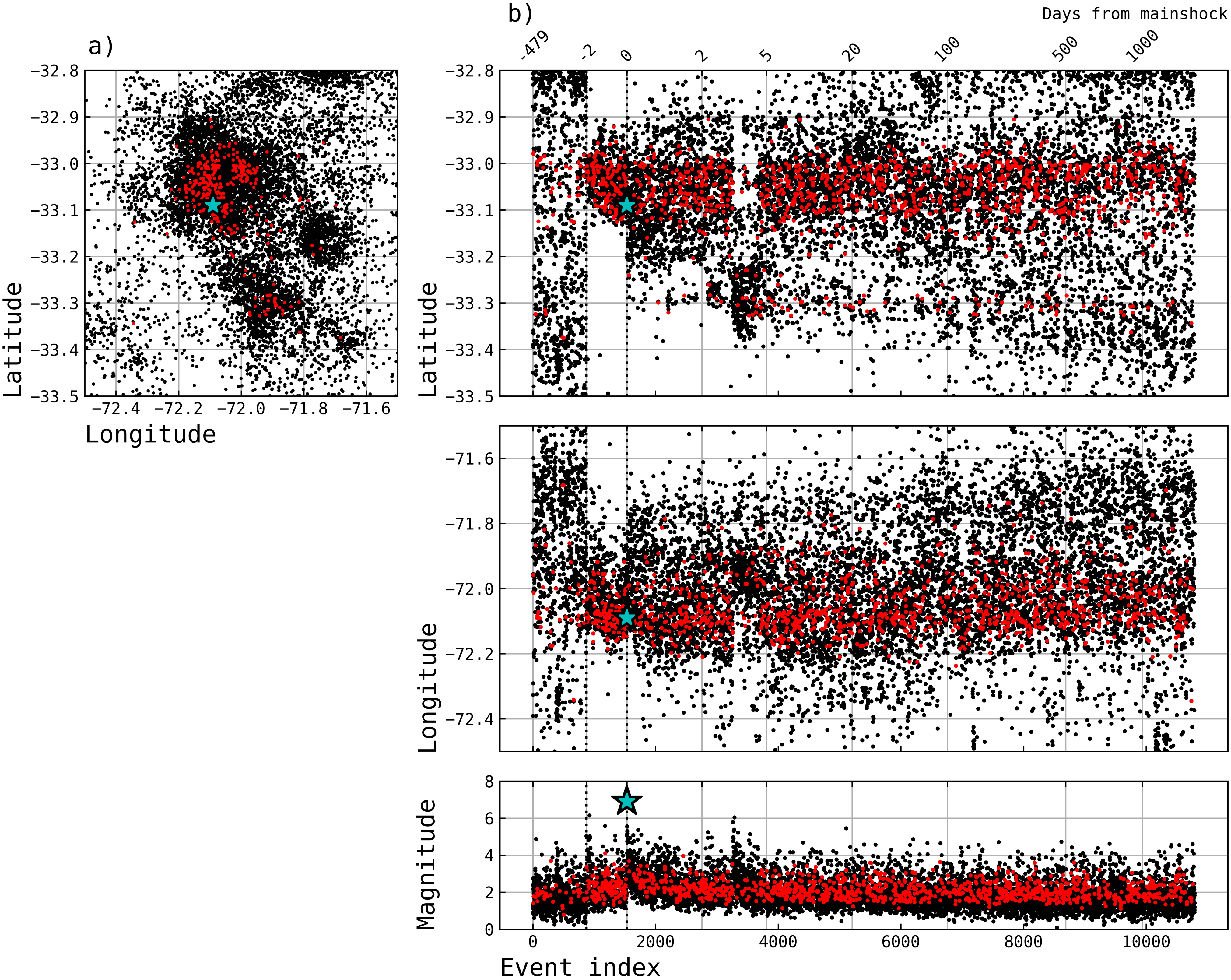

a)
b)
Days from mainshock
-479
-2
0
2
5
20
100
500
1000
Latitude
Longitude
Magnitude
Event index
-32.8
-32.9
-33.0
-33.1
-33.2
-33.3
-33.4
-33.5
-72.4
-72.2
-72.0
-71.8
-71.6
0
2
4
6
8
0
2000
4000
6000
8000
10000

Figure 7.

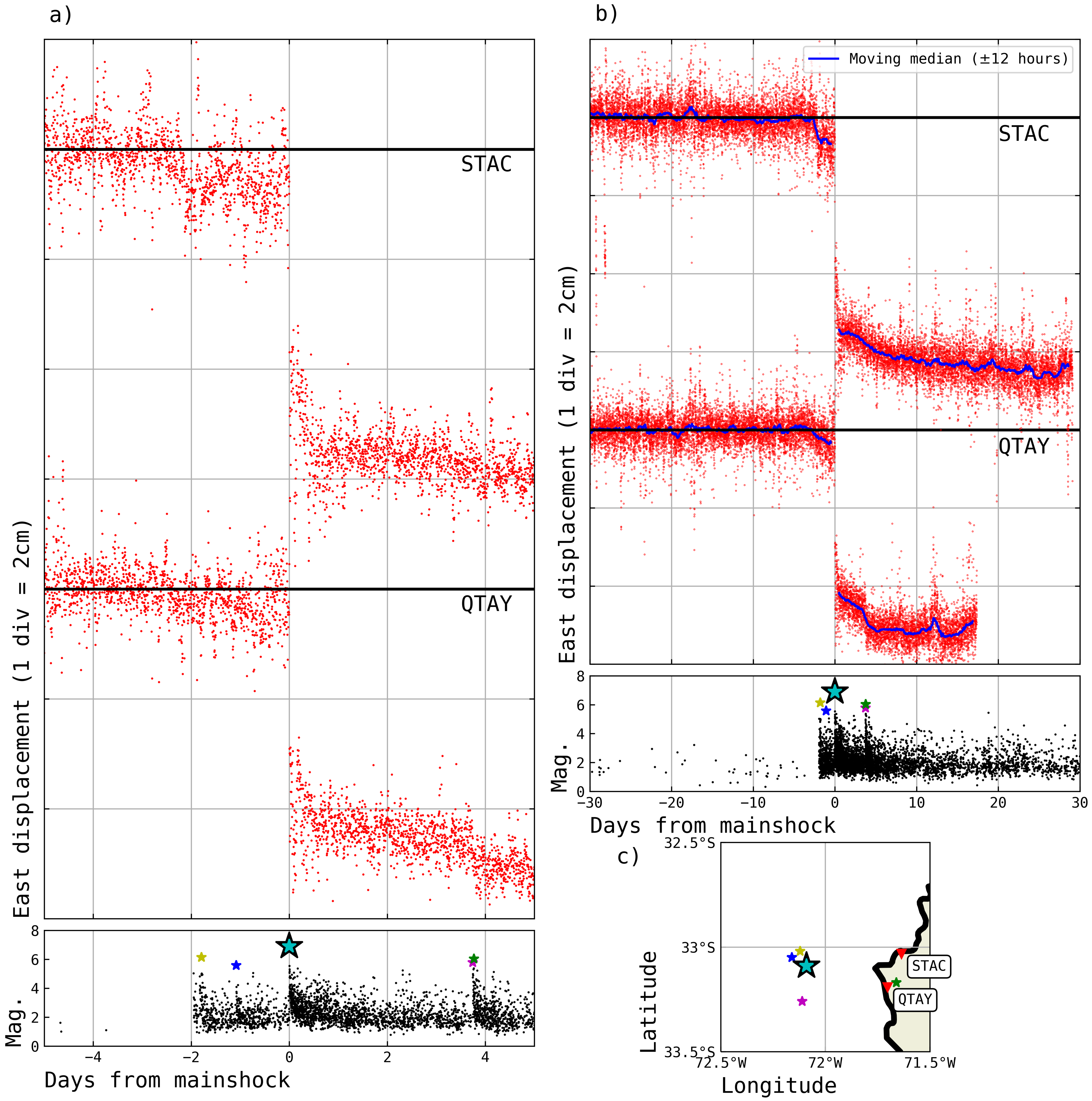

a)
b)
c)
STAC
QTAY
Moving median (±12 hours)
East displacement (1 div = 2cm)
Mag.
Days from mainshock
−30
−20
−10
0
10
20
30
−4
−2
0
2
4
0
2
4
6
8
32.5°S
33°S
33.5°S
72.5°W
72°W
71.5°W
Latitude
Longitude